arXiv:1605.02359v1 [astro-ph.SR] 8 May 2016

An algorithm for computing the 2D structure of fast rotating stars

Michel Rieutord[a,b], Francisco Espinosa Lara[1 a,b], Bertrand Putigny[a,b]

[a] *Université de Toulouse; UPS-OMP; IRAP; Toulouse, France*
[b] *CNRS; IRAP; 14, avenue Edouard Belin, F-31400 Toulouse, France*

Abstract

Stars may be understood as self-gravitating masses of a compressible fluid whose radiative cooling is compensated by nuclear reactions or gravitational contraction. The understanding of their time evolution requires the use of detailed models that account for a complex microphysics including that of opacities, equation of state and nuclear reactions. The present stellar models are essentially one-dimensional, namely spherically symmetric. However, the interpretation of recent data like the surface abundances of elements or the distribution of internal rotation have reached the limits of validity of one-dimensional models because of their very simplified representation of large-scale fluid flows. In this article, we describe the ESTER code, which is the first code able to compute in a consistent way a two-dimensional model of a fast rotating star including its large-scale flows. Compared to classical 1D stellar evolution codes, many numerical innovations have been introduced to deal with this complex problem. First, the spectral discretization based on spherical harmonics and Chebyshev polynomials is used to represent the 2D axisymmetric fields. A nonlinear mapping maps the spheroidal star and allows a smooth spectral representation of the fields. The properties of Picard and Newton iterations for solving the nonlinear partial differential equations of the problem are discussed. It turns out that the Picard scheme is efficient on the computation of the simple polytropic stars, but Newton algorithm is unsurpassed when stellar models include complex microphysics. Finally, we discuss the numerical efficiency of our solver of Newton iterations. This linear solver combines the iterative Conjugate Gradient Squared algorithm together with an LU-factorization serving as a preconditionner of the Jacobian matrix.

Keywords: Astrophysics - Stellar Models

1. Introduction

The recent progress of observational stellar astrophysics in spectroscopy, spectropolarimetry or interferometry have called for more realistic models of stars, with a focus on the effects of rotation. Without rotation stars may be modeled as spherical 'balls' with a detailed microphysics: equation of state, opacities or nuclear reaction rates have been the subject of intense research over the past fifty years (e.g. Maeder, 2009; Kippenhahn et al., 2012). In these one-dimensional models, the main difficulty comes from the modeling of the averaged heat transport by convection in the various parts of the star where hydrostatic equilibrium is unstable. For stars burning hydrogen on the so-called main sequence, these regions are a convective core when the stellar

[1] Present address: Space Research Group, University of Alcalá, 28871 Alcalá de Henares, Spain

mass is larger than 1.3 solar mass - hereafter noted $M_\odot$ - and a convective envelope when the mass is less than 1.8 $M_\odot$. One-dimensional models have been designed and redesigned for more than fifty years now and are still widely used (e.g. the code MESA started by Paxton et al. 2011). They have had great successes in depicting a now widely accepted view of stellar evolution.

But, as alluded above, the more precise observations obtained with modern instruments show details that are difficult to explain with one-dimensional, spherically symmetric models. Most of these details are related to fluid flows in the stars. We easily understand that it is uneasy to model fluid flows in one dimension. The bulk effects of rotation are the first victims of an imposed spherical symmetry. Current one-dimensional codes, like MESA or CESAM (Morel, 1997), include a modeling of rotation through its average effects: these are mainly the centrifugal effect and radial differential rotation that mimic baroclinic flows. As expected, these models show discrepancies when compared to observational data. For instance, they have difficulties to reproduce the abundances of elements at the surface of stars (Brott et al., 2011) or they simply cannot be used to interpret interferometric observations of fast rotating stars (e.g. Monnier et al., 2007).

To overcome these difficulties, the natural step forward is to relax the spherical symmetry in the modeling and to work with models owing two dimensions of space at least. Thus, fluid flows can be computed more realistically and rotational effects as well. The first step in this direction is to elaborate two-dimensional axisymmetric models of stars. The centrifugal distortion of the star can then be naturally included as well as the global steady flows.

Attempts to build such models have begun in the sixties (James, 1964), almost at the same time as 1D models. First steps in the quest of 2D stellar models for fast rotating stars have been marked by a series of works starting with the one of Ostriker and Mark (1968) who introduced the Self-Consistent Field (SCF) method[2](see Rieutord, 2006b, for a short historical review). In a subsequent series of papers, Clement (1974, 1978, 1979, 1994) proposed another way of solving Poisson's equation by using finite differences, while later on Eriguchi and Müller (1985, 1991) introduced a linear mapping $r_i(\theta_k) = \zeta_i R_s(\theta_k)$ such that the grid $r_i(\theta_k)$ automatically adjusts to the shape of the star (here given by its colatitude dependent radius $R(\theta)$). More recently, Roxburgh (2004, 2006) reconsidered 2D models of fast rotating stars for asteroseismic purposes, while Jackson et al. (2004, 2005) reconsidered similar models for interpreting the very flattened shape of the Be star Achernar, as revealed by the first precise interferometric observations of this star (Domiciano de Souza et al., 2003). At the same time, Jackson et al. (2004, 2005) improved the SCF method. Recent results of MacGregor et al. (2007) presented SCF models with very high angular momentum showing stellar models with very strongly distorted shapes compared to the sphere. In an other line of research, Deupree (2011) also computed 2D models that he later used to interpret recent interferometric and asteroseismic data obtained for the nearby fast rotating star Rasalhague (e.g. Deupree et al., 2012). However, in all the foregoing work the internal rotation of the star had to be specified (either as a solid body rotation or as a given differential rotation). In real isolated stars, differential rotation emerges from the baroclinic torque and Reynolds stresses, the former being prominent in radiative zones and the latter in convective regions. The first

[2]Briefly, this method use's the formal solution of Poisson's equation in term of the density distribution, i.e.

$$\phi(\mathbf{x}) = -G \int \frac{\rho(\mathbf{x}')}{|\mathbf{x} - \mathbf{x}'|} d^3\mathbf{x}'$$

which has the great advantage of including the boundary conditions on ϕ at infinity. The potential is used to find a new ρ itself leading to a new potential.

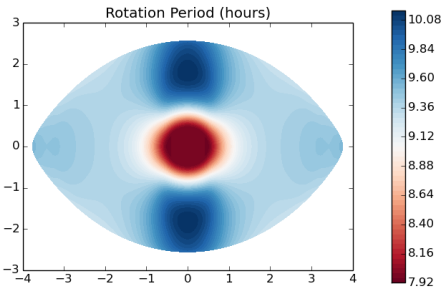

Figure 1: Meridional cut of a $5M_{\odot}$ 2D ESTER (stellar) model showing the internal differential rotation of the star. The equatorial velocity is 95% of the break-up velocity. Dark blue is for low angular velocity and red for high angular velocity (core region). The side length scale unit is the solar radius.

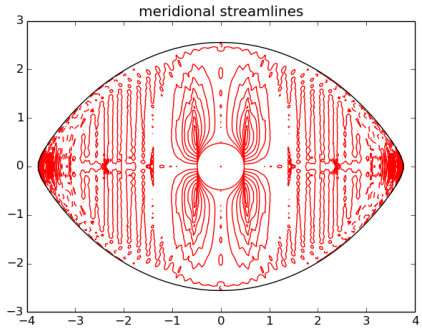

Figure 2: Streamlines associated with the meridional circulation for the same model and as in figure 1.

models that included self-consistently the pressure, density, temperature distributions and the associated baroclinic torque have been presented in Espinosa Lara and Rieutord (2007) and later, using the proper spheroidal geometry, in Rieutord and Espinosa Lara (2009); Espinosa Lara and Rieutord (2013).

The main difficulty was to find the appropriate algorithm that allowed convergence of the iterations to the quasi-steady state of a fast rotating star consistently with the mean flows that pervade the whole star. Indeed, these flows face extremely large density variations (typically eight orders of magnitude) making solutions prone to numerical instabilities. In addition, heat transfer depends on the strongly varying heat conductivity (controlled by the fluid opacity) or on a vigorous turbulent convection. Even if thermal convection is modeled by a smooth mean-field approach, the global rapid variations of transport coefficients, especially near the surface, make the problem thorny.

The aim of this paper is to present to the readers the numerical side of the solution that we have found to the modeling of fast rotating main sequence stars as illustrated in Fig. 1 and 2. This solution is now used in the ESTER code, which is freely available at http://ester-project.github.io/ester/. A detailed discussion of the physical and astrophysical hypothesis of the ESTER models may be found in Espinosa Lara and Rieutord (2013) or Rieutord and Espinosa Lara (2013). In the following, we shall first present the set of equations to be solved (sect. 2) and continue on presenting the mapping that is used to deal with the spheroidal shape of the star (sect. 3). We then introduce our choice of the discretization (spectral methods) in section 4 and discuss the choice of the algorithm (sect. 5). We finally illustrate the results with examples

showing the numerical efficiency of the ESTER code at computing various stellar models (sect. 6). Conclusions and outlooks end the paper.

2. Mathematical formulation

2.1. Equations of stellar structure

Basically equations that are governing the structure of stars are those governing a compressible self-gravitating fluid flow with heat sources. Because of the very high temperatures of the central regions, heat sources are coming from nuclear reactions. The (quasi) steady state is possible because the star cools through radiation at its surface usually assumed as a black body. This is not a strict steady state because nuclear reactions slowly change the chemical composition of the star leading to higher and higher densities at the center. However, on the main sequence, the time scale of hydrogen nuclear burning is sufficiently long compared to all dynamical time scales so that the steady state is a very good approximation. The present work restrict to this period of the life of stars.

Let us now present the four partial differential equations that govern this steady state.

2.1.1. Gravitational potential

Self-gravity is governed by Poisson's equation

$$\nabla^2\phi = 4\pi G\rho \tag{1}$$

where ϕ is the gravitational potential, ρ is the density and G the gravitational constant. This equation is completed by boundary conditions that state that ϕ is regular at the center of the star and vanishes at infinity.

2.1.2. Dynamics

Two equations govern the mean velocity field in the star. Indeed, we are only interested in the average steady state of the star and therefore turbulent flows are only represented by their mean-fields. Hence, everywhere in the following, $\mathbf{v}$ should be understood as a mean velocity field. Moreover, no magnetic field is considered. Mass conservation yields

$$\nabla\cdot(\rho\mathbf{v}) = 0 \tag{2}$$

while the momentum conservation requires

$$\rho\mathbf{v}\cdot\nabla\mathbf{v} = -\nabla P - \rho\nabla\phi + \mathbf{F}_v \tag{3}$$

in an inertial frame. In these equations, $P(\mathbf{r})$ is the mean pressure and $\rho(\mathbf{r})$ the mean density. The viscous force $\mathbf{F}_v$ includes, whenever necessary, the turbulent Reynolds stresses. It is taken into account in order to remove the degeneracy of the inviscid problem (e.g. Espinosa Lara and Rieutord, 2013, and below). For later use, we recall that the equatorial angular velocity is bounded by the keplerian angular velocity at equator, namely

$$\Omega_k = \sqrt{\frac{GM}{R_{\rm eq}^3(\Omega_k)}} \tag{4}$$

We shall call this quantity the critical angular velocity. The dependance $R_{\rm eq}(\Omega_k)$ underlines that the equatorial radius depends on the angular velocity at equator, hence the determination of the critical angular velocity needs the solution of an involved nonlinear problem.

2.1.3. The temperature field

The equation of energy or of entropy S gives the temperature field. We write it as

$$\rho T \mathbf{v} \cdot \nabla S = -\nabla \cdot \mathbf{F} + \varepsilon_* \tag{5}$$

where the heat flux is

$$\mathbf{F} = -\chi \nabla T + \mathbf{F}_{\rm conv} \tag{6}$$

namely the sum of the radiative flux and the convective flux when thermal convection sets in. In these equations, $\varepsilon_* \equiv \varepsilon_*(\rho, T)$ is the heat power generated by nuclear reactions per unit volume and $\chi \equiv \chi(\rho, T)$ is the heat conductivity.

Convective zone boundaries are determined by the Schwarzschild criterion. Namely, we associate convectively stable regions with those verifying

$$-\mathbf{g}_{\rm eff} \cdot \nabla S > 0$$

Note that our models have a chemically homogeneous core and envelope. Thus Ledoux criterion does not apply and our model do not deal with semi-convection.

The convective flux needs being modeled by a mean-field approach. Presently, no general model exist. One dimensional models have shown that the convective core of massive or intermediate-mass stars is almost isentropic. We therefore assume perfect isentropy in stellar convective cores. Elsewhere, and in particular in stellar envelopes, convection is not efficient enough to impose isentropy everywhere. In 1D models, one uses the mixing length theory (Maeder, 2009), but this approach has not yet been generalized to a 2D set-up. Thus, we shall ignore at the moment stars with convective envelopes. This restricts the model applications to main-sequence stars of high or intermediate mass (the so-called early-type stars whose mass is typically larger than 2 $M_\odot$). In these stars surface convection may exist but it is inefficient and does not affect the stellar structure.

2.2. Boundary conditions

The foregoing partial differential equations need to be completed by boundary conditions. At the star's center we just need to impose the regularity of the fields. At the stellar surface the situation is more complicated. First, we need to define the stellar surface.

2.2.1. The stellar surface

As in 1D models we define the stellar surface as given by a fixed optical depth. We recall that the optical depth is a non-dimensional quantity, usually called τ, defined by

$$\tau(z, \nu) = \int_z^\infty \alpha_\nu(z') dz'$$

Here, $\alpha_\nu(z')$ is the absorption coefficient at the altitude z' and at the (electromagnetic) frequency ν. Usually, a grey atmosphere model is adopted to avoid the frequency dependence. Typically, the surface of the star is defined as the surface where the grey optical depth is 2/3 (Hansen and Kawaler, 1994). With a simple model of the atmosphere (e.g. Espinosa Lara and Rieutord, 2013), this surface is replaced by an isobar whose pressure is determined at the pole of the star (see below).

2.2.2. The pressure and temperature boundary conditions

The pressure is determined through its gradient in the momentum equation (3). Hence, it is known up to a constant. This constant actually fixes the extension of the star and thus its radius. To be consistent with spherically symmetric models we fix the pressure constant by assuming that the polar pressure is given by

$$P_s = P_{\rm pole} = \tau_s \frac{g_{\rm pole}}{\kappa_{\rm pole}}, \tag{7}$$

where τ_s is the chosen optical depth (usually 2/3), $g_{\rm pole}$ is the polar gravity and $\kappa_{\rm pole}$ is the polar opacity (opacity is related to the absorption coefficient by $\kappa = \alpha/\rho$). Relation (7) is derived from a simplified hydrostatic model of the atmosphere of stars (e.g. Kippenhahn et al., 2012).

Once the polar pressure is defined by (7), the associated isobar is taken as the surface of the stellar model. This surface coincides with the photospheric surface of the star at the pole only and is below the photospheric surface elsewhere. To take into account the fluid above this isobar, we model this fluid layer by a locally polytropic atmosphere. Namely, we say that in this atmosphere

$$P = P_{\rm pole}(1 - z)^{n+1} \tag{8}$$

where n is the polytropic index and z a scaled height in the atmosphere. With (8), we can set the true surface at $z = 0$ at the pole and at $z(\theta)$ elsewhere. At the true surface, where the optical depth equals τ_s the pressure is

$$\tau_s \frac{g_{\rm eff}(\theta)}{\kappa(\theta)}$$

and $z(\theta)$ is such that

$$1 - z(\theta) = \left(\frac{g_{\rm eff}(\theta)\kappa_{\rm pole}}{g_{\rm pole}\kappa(\theta)} \right)^{1/(n+1)}.$$

Using the fact that the temperature varies like $1 - z$ in a polytropic atmosphere, and that the temperature equals the effective temperature at optical depth τ_s, we find that the temperature must verify

$$T = T_s(\theta) = T_{\rm eff}(\theta) \left(\frac{g_{\rm pole}\kappa(\theta)}{g_{\rm eff}(\theta)\kappa_{\rm pole}} \right)^{1/(n+1)} \tag{9}$$

on the isobar $P = P_{\rm pole}$. We note that according to this definition, T_s(pole) is also the polar effective temperature of the stellar model. Hence, along with the regularity of the temperature field at the star's center, the condition

$$T = T_s(\theta) \qquad \text{at the surface}$$

fully defines the temperature field inside the stellar model (Espinosa Lara and Rieutord, 2013). For applications below, we set the polytropic index to $n = 3$, a value adapted to a radiative layer.

2.2.3. Velocity boundary conditions

The natural boundary conditions for the velocity field at the surface of the star are the stress-free conditions. Indeed, the neglected layers actually impose a negligible stress on the surface (this simplified view may however be challenged in real stars by a combination of winds and magnetic fields). These conditions read:

$$\mathbf{v} \cdot \mathbf{n} = 0 \quad \text{and} \quad ([\sigma]\mathbf{n}) \wedge \mathbf{n} = \mathbf{0} \tag{10}$$

where $[\sigma]$ is the stress tensor and $\mathbf{n}$ the outer normal of the stellar surface. Actually, we have to take into account the additional constraint that the equatorial velocity is given as needed to fix the rotational velocity of the star, namely

$$v_\varphi(r = R_{\rm eq}, \theta = \pi/2) = V_{\rm eq} \tag{11}$$

2.2.4. Dealing with viscosity

The boundary conditions on the velocity (10) are numerically costly because in stellar conditions thin boundary (Ekman) layers develop at the surface. However, simplifying these conditions by just neglecting viscosity altogether is not possible. Indeed, it is well-known that the inviscid problem is degenerate (e.g. Rieutord, 2006a). Using (3), imposing axisymmetry and neglecting the viscous force, we get the so-called thermal wind equation (Greenspan, 1968), which here reads

$$s\frac{\partial \Omega^2}{\partial z} = \mathbf{e}_\varphi \cdot \frac{\nabla p \times \nabla \rho}{\rho^2} \ , \tag{12}$$

where $\Omega \equiv \Omega(s, z)$ is the local angular velocity and (s, z, φ) are the cylindrical coordinates. We easily see that this equation is invariant in the transformation $\Omega^2 \to \Omega^2 + \Omega_g^2(s)$ for any $\Omega_g(s)$. The condition imposing the equatorial velocity (11) is not sufficient to lift the degeneracy. Actually, the same problem arises when one considers the steady baroclinic flows in a rotating frame (e.g. Rieutord, 2006a). Hence, viscosity plays a fundamental role in the determination of the differential rotation of a star (especially in the radiative regions), but it brings new very thin boundary layers that make the problem more difficult numerically. However, using the results of Rieutord (2006a), Espinosa Lara and Rieutord (2013) have devised a new (nonlinear) boundary condition for $\Omega(s, z)$ that couples this quantity with the stream function of the meridian circulation, and which avoids the computation of the Ekman layers. This boundary condition reads

$$\mu s^2 \hat{\xi} \cdot \nabla\Omega + \psi \hat{\tau} \cdot \nabla(s^2\Omega) = 0 \qquad \text{on the surface} \ . \tag{13}$$

where μ is the dynamical viscosity and $\hat{\xi}$ is a unit vector perpendicular to the surface while $\hat{\tau}$ is a unit vector tangent to it. ψ is the stream function of the meridional flow $\mathbf{u}$, such that $\rho\mathbf{u} = \nabla \times (\psi\hat{\varphi})$, $\hat{\varphi}$ being the azimuthal unit vector. The derivation of (13) is quite tedious and we refer the reader to Espinosa Lara and Rieutord (2013) for the details. Thus doing, viscosity (if small enough!) can be taken into account for the determination of the azimuthal velocity $v_\varphi(r, \theta)$ and the associated angular velocity $\Omega(r, \theta)$, without including explicitly the viscous force in the meridional part of the momentum equation. Hence, the meridional part of the momentum equation (3) reduces to Euler's equation

$$\rho s\Omega^2 \mathbf{e}_s = \nabla p + \rho\nabla\phi \tag{14}$$

taking into account the axisymmetry of the fields and the vanishing of the meridian circulation with viscosity (e.g. Busse, 1981; Rieutord, 2006a). Although the variables are all strongly coupled, we may consider (14) as the equation determining the pressure field.

The φ-component of (3), controls the balance of the flux of angular momentum and determines the meridional velocity (along with mass conservation) forced by the viscous stress generated by the (previously derived) differential rotation. It reads

$$\nabla \cdot (\rho s^2 \Omega \mathbf{u}) = \nabla \cdot (\mu s^2 \nabla \Omega) \tag{15}$$

where $\mathbf{u}$ is the meridional circulation and μ the dynamical viscosity. For simplicity we here assume that shear stresses are represented by a mere (newtonian) viscous force, but in principle more elaborated Reynolds stress models can be used. Equation (15) may be understood as the one used to derive the stream function ψ of the meridional circulation. From (15), we now see that the profile of viscosity μ influences the shape of the meridional circulation and through (13), the differential rotation. However, the amplitude of the viscosity (in the limit of vanishing Ekman numbers) has no importance for the shape of the flow field (see below).

The foregoing treatment of the effects of viscosity has the merit of eliminating the small scale induced by the Ekman layer, while removing the degeneracy of the inviscid limit. There is however a price to pay: the elimination of the viscous effects in the meridional component of the momentum equation (14) also eliminates the (viscous) Stewartson layer that naturally arises on the tangent cylinder circumventing the convective core (e.g. Espinosa Lara and Rieutord, 2013). More work is needed to find a way to take into account such a dynamical feature, which presumably plays a role in the transport of chemical elements, while preserving the numerical stability of the solutions.

2.3. Microphysics

Beside the foregoing partial differential equations and their associated boundary conditions, one needs to specify the equations of state of the fluid, the dependence of the radiative conductivity with temperature and density, and the power of nuclear reactions. As far as the equation of state and the opacity are concerned (the opacity controls the radiative conductivity), we use the OPAL tables of Rogers et al. (1996), which give the relations

$$P \equiv P(\rho, T) \tag{16}$$

$$\chi \equiv \chi(\rho, T) \tag{17}$$

as well as other thermodynamics quantities.

For the nuclear heat power, we use an analytic formula that accounts for the heat generation by hydrogen fusion either by the pp-chains or by the CNO cycle (each dominating in some range of temperatures). For that we set

$$\varepsilon_* = \varepsilon_*^{\rm pp} + \varepsilon_*^{\rm CNO} \tag{18}$$

with

$$\varepsilon_*^{\rm pp} = \varepsilon_0^{\rm pp} X^2 \rho^2 T_9^{-2/3} \exp\left(-\frac{A_{\rm pp}}{T^{1/3}}\right) . \tag{19}$$

This expression is also used by the CESAM code (Morel and Lebreton, 2008). Similarly,

$$\varepsilon_*^{\rm CNO}(\rho,T) = \varepsilon_0^{\rm CNO} X X_{\rm CNO} \rho^2 T_9^{-2/3} \exp\left(-\frac{A_{\rm CNO}}{T^{1/3}}\right) \times \left(1 + 0.027 T_9^{1/3} - 0.778 T_9^{2/3} - 0.149 T_9\right), \tag{20}$$

using the expression given in Kippenhahn and Weigert (1990)[3]. In these expressions $T_9 = T/10^9$, X is the hydrogen mass fraction, $X_{\rm CNO} \simeq Z/2$ is the mass fraction of CNO elements assumed to be a solar mixture of metallicity Z (e.g. Maeder, 2009). The constants are taken as:

$$\varepsilon_0^{\rm pp} = 8.24 \times 10^4 \text{ cgs}, \qquad \varepsilon_0^{\rm CNO} = 8.67 \times 10^{25} \text{ cgs}, \qquad A_{\rm pp} = 3600., \quad A_{\rm CNO} = 1.5228 \times 10^4$$

but detailed nuclear reaction rates can be obtained from the NACRE compilation (Angulo et al., 1999; Xu et al., 2013).

2.4. Integral constraints

The foregoing equations are completed by one integral constraint, namely the one that specifies the mass of the star

$$M = \int_{(V)} \rho dV \ . \tag{21}$$

If needed, the total angular momentum

$$\mathbf{L} = \int_{(V)} \rho \mathbf{r} \times \mathbf{v} dV \tag{22}$$

can also be imposed, but in such a case this constraint replaces the fixed equatorial velocity (11).

2.5. Scaled equations

In order to solve the foregoing set of equations, we first scale the equations so as to use, when possible, non-dimensional variables.

We choose to scale pressure, density and temperature by their central values and other quantities as follows:

Length scale ≡ polar radius	R
Pressure scale ≡ central pressure	P_c
Density scale ≡ central density	ρ_c
Temperature scale ≡ central temperature	T_c
Gravitational potential scale	P_c/ρ_c
Angular velocity scale	$\frac{1}{R}\sqrt{\frac{P_c}{\rho_c}}$
Meridional velocity scale	$E\sqrt{\frac{P_c}{\rho_c}}$

where E is the Ekman number defined as

[3] Kippenhahn et al. (2012) give a more recent expression of the CNO-cycle power but the difference with the "old" expression is negligible for our purpose.

$$E = \frac{\mu_c}{\rho_c \Omega_0 R^2} \qquad \text{with} \qquad \Omega_0 = \sqrt{\frac{P_c}{R^2 \rho_c}} \,. \tag{23}$$

With these scalings, Poisson's equation now reads:

$$\nabla^2 \phi = \pi_c \rho \qquad \text{with} \qquad \pi_c = \frac{4\pi G \rho_c^2}{P_c} \tag{24}$$

The scaled equation of angular momentum reads

$$\nabla \cdot (\rho s^2 \Omega \mathbf{u}) = \nabla \cdot (\mu s^2 \nabla \Omega) \tag{25}$$

where $\mu \equiv \mu(r, \theta)$ is the normalized viscosity profile. As a first step, and in the following, we simply take $\mu = 1$.

With the foregoing scalings, we note that the meridional circulation is very small compared to the differential rotation. Indeed, from (25) we see that $\|\mathbf{u}\| \sim \Omega \sim 1$, but dimensional velocities are such that $\|\mathbf{v}_{\rm merid}\|/V_\varphi \sim E$, while in fast rotating stars $E \lesssim 10^{-8}$ (e.g. Espinosa Lara and Rieutord, 2013). Hence, the scaled meridional circulation together with boundary conditions (13), which now reads

$$s^2 \hat{\xi} \cdot \nabla \Omega + \psi \hat{\tau} \cdot \nabla (s^2 \Omega) = 0 \qquad \text{on the surface} \tag{26}$$

with scaled variables, allows us to set $E = 0$ without introducing an undetermined function in the solution.

Another benefit of taking the limit $E = 0$ is that it eliminates heat advection in the energy-entropy equation solved in radiative regions. Such limit is indeed equivalent to setting the Prandtl number to zero which stresses that heat is more efficiently transported by diffusion than by advection in a radiative region (see a recent discussion of the dynamics of rotating radiative regions in Rieutord, 2006c). Hence, the energy equation can be simplified as

$$\nabla^2 T + \nabla \ln \chi \cdot \nabla T + \Lambda \frac{\varepsilon_*}{\chi_*} = 0 \qquad \text{with} \qquad \Lambda = \frac{\rho_c R^2}{T_c} \tag{27}$$

Note that Λ is a dimensional constant since ε_* and χ_* are of different dimensions.

While (27) is solved to give the temperature field in radiative zones, convective regions need a specific treatment. Presently, our solutions only handle convective cores where we impose

$$\nabla S = \mathbf{0} \tag{28}$$

with S being the entropy. Such an equation assumes that convection is extremely efficient so as to impose a constant entropy everywhere in the convective region. This is actually the case in stellar convective cores according to the mixing-length model (Maeder, 2009). In convective envelopes, like that of the Sun, the efficiency of convection decreases very much near the stellar surface and (28) is no longer appropriate. A new approach is needed, but it is beyond the scope of the present work. Thus, as mention in the introduction, the present numerical solutions only apply to main-sequence early-type stars, since these stars own a convective core (due to a powerful nuclear heating), but no or a very small convective envelope.

To finish with the scaled equation, we note that the momentum equation (14) and the vorticity equations (12) are unchanged (except that they use scaled variables). Mass conservation also remains the same

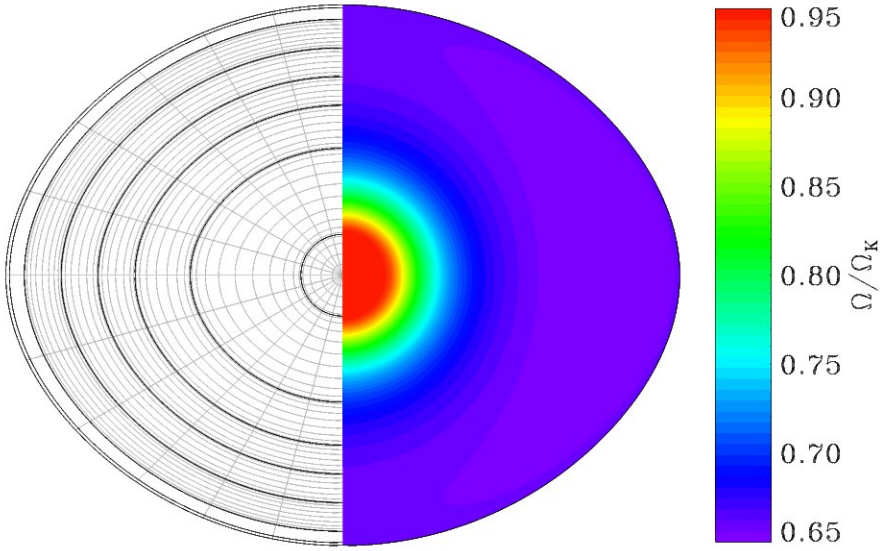

Figure 3: Left: plot of the computational grid inside the star. The solid thick lines show the frontiers of the domains. The outer grid is not represented. Right: just for illustration, the associated differential rotation of the computed stellar model with parameters M=3 $M_\odot$ and $\Omega/\Omega_c = 0.7$ leading to a flatness of 20%. The chemical composition is homogeneous and solar. (Credit Daniel Reese)

$$\nabla \cdot (\rho \mathbf{u}) = 0 \tag{29}$$

3. The mapping

One of the difficulties of this problem is the *a priori* unknown shape of the star. Hence, we devised a method where the grid evolves with iterations so as to always fit the surface of the star where boundary conditions are applied.

3.1. An adapted system of coordinates

We therefore construct a mapping which connects the usual spherical coordinates (r, θ, φ) to new spheroidal coordinates $(\zeta, \theta'\varphi')$ such that the surface $\zeta = 1$ describes the surface of the star. Therefore the mapping reads:

$$\begin{cases} r = r(\zeta, \theta') \\ \theta = \theta' \\ \varphi = \varphi' \end{cases} \tag{30}$$

The problem reduces to that of finding a suitable form for the function $r(\zeta, \theta)$.

However, the mapping needs to be a little more sophisticated. Indeed, we also need to solve Poisson's equation outside the star since the gravitational field is not simple in this domain. Thus,

the computational domain should be at least divided into two parts: the star and the surrounding vacuum. But our choice of a spectral method (see below) makes the use of a multidomain method attractive also inside the star. It indeed turns out that a spectral solver deals more easily with the dramatic variations of density between the center and the surface of the star when these density variations are distributed over several domains. Thus, we split the star into n-spheroidal shells. More precisely, we distribute the domains so that the pressure ratio (between the upper and lower boundaries of the domain) is almost the same in every domains. Thus, we easily deal with the changing pressure scale height within the star. The domain boundaries can also be attached to discontinuities that arise from the physics of the star (chemical barriers, jumps in thermal gradients, etc).

Hence, we divide the domain $\mathcal{D}$ into n subdomains $\{\mathcal{D}_i\}$, the frontiers of which are given by a series of functions $\{R_i(\theta), i = 0, n-1\}$ such that the domain $\mathcal{D}_i$ is bounded by the spheroids

$$r = R_i(\theta) \qquad \text{and} \qquad r = R_{i+1}(\theta)$$

where $R_0(\theta) = 0$ is the center of the star and $R_n(\theta) = R(\theta)$ is the stellar surface. We also use an external domain $\mathcal{D}_{ex}$ that extends from the outer boundary $R_n(\theta)$ to infinity. In this latter domain, we only solve Poisson's equation. This additional domain allows us to impose conveniently the vanishing of the gravitational potential at infinity. In Fig. 3 we give an example of the grid structure that is used inside the star together with the differential rotation associated with the solution.

3.2. The details of the mapping

Inspired by the work of Bonazzola et al. (1998), we choose the following form of the mapping in the stellar domains $\mathcal{D}_i$

$$r(\zeta,\theta) \equiv r_i(\zeta,\theta) = a_i\xi\Delta\eta_i + R_i(\theta) + A_i(\xi)(\Delta R_i(\theta) - a_i\Delta\eta_i) \qquad \text{for } \zeta \in [\eta_i, \eta_{i+1}] \qquad (31)$$

where the $a_i's$ are constants and where we have defined:

$$\begin{aligned}
\eta_i &= R_i(\theta = 0) \\
\Delta\eta_i &= \eta_{i+1} - \eta_i \\
\Delta R_i(\theta) &= R_{i+1}(\theta) - R_i(\theta) \\
\xi &= \frac{\zeta - \eta_i}{\Delta\eta_i} \quad \text{so that} \quad 0 \le \xi \le 1 \quad \text{when} \quad \zeta \in [\eta_i, \eta_{i+1}]
\end{aligned}$$

Since the polar radius is chosen as the unit length, $R(0) \equiv R_n(0) = 1$ and $\eta_n = 1$. Hence, the star is scanned when $\zeta \in [0, 1]$. Note that the ξ variable is a local radial variable specific to each domain. The mapping in the outer empty domain surrounding the star will be discussed below.

The $A_i(\xi)$ functions verify

$$A_i(0) = 0 \qquad \text{and} \qquad A_i(1) = 1$$

so that

$$r(\eta_i, \theta) = R_i(\theta)$$

but are otherwise arbitrary.

A simple choice of the A_i-functions would be $A_i(\xi) = \xi$ so that the mapping is linear, namely

$$r(\zeta, \theta) = R_i(\theta) + \xi \Delta R_i(\theta) \qquad \text{for} \qquad \xi \in [0, 1] \qquad \text{and} \qquad \zeta = \eta_i + \xi \Delta \eta_i \tag{32}$$

If the star is described by a single domain, then

$$r(\zeta, \theta) = \xi R(\theta) \tag{33}$$

This is the mapping that was chosen by Eriguchi and Müller (1985, 1991). However, as noticed by Eriguchi and Müller (1985) and Bonazzola et al. (1998), this linear mapping requires a special treatment of the center. This is why Bonazzola et al. (1998) suggested to use a nonlinear mapping based on a higher order polynomial for the A_i-functions. Hence, following this latter work, we choose

$$A_0(\xi) = (5\xi^3 - 3\xi^5)/2 \tag{34}$$

$$A_i(\xi) = 3\xi^2 - 2\xi^3 \qquad \text{for } i = 1, \ldots, n-1 \tag{35}$$

This choice is such that near the center of the star, the (ζ, θ, φ) coordinates reduce to the spherical coordinates (r, θ, φ). This property allows us to use the properties of polynomial regularity of functions expanded over spherical harmonics. Central boundary conditions can thus be imposed without numerical difficulties.

The a_i constants are arbitrary and should be optimized for the problem at hands. Here, they are chosen so that $r(\zeta, \theta)$ is an increasing function of ζ and so as to avoid a singular mapping. The Jacobian of the mapping is

$$J = \left| \begin{array}{cc} \frac{\partial r}{\partial \zeta} & \frac{\partial r}{\partial \theta'} \\ \frac{\partial \theta}{\partial \zeta} & \frac{\partial \theta}{\partial \theta'} \end{array} \right| = \frac{\partial r}{\partial \zeta} \equiv r_\zeta$$

We first observe that:

$$A_i'(\xi) = 6\xi(1 - \xi) \qquad \text{and} \qquad A_0' = \frac{15}{2}\xi^2(1 - \xi^2) \tag{36}$$

Hence, $A_i'(0) = A_i'(1) = 0$, and

$$J = a_i + A_i'(\xi)\left(\frac{\Delta R_i(\theta)}{\Delta \eta_i} - a_i\right)$$

in domain $\mathcal{D}_i$. From the foregoing expressions of A_i', we note that $A_i'(\xi) \geq 0$ in each domain. On the other hand, the thickness of each domain, namely $\Delta R_i(\theta)$, can be chosen as an increasing function of θ from pole to equator. This is indeed always possible as rotating stars are oblate, namely with an equatorial radius larger than the polar radius. Hence, we can choose the $R_i(\theta)$ such that

$$\Delta R_i(\theta) \geq \Delta \eta_i, \qquad \forall\ \theta \in [0, \pi]\ .$$

Thus, if we choose

$$a_i = 1$$

we are insured that

$$J(\zeta, \theta) \geq 1 \qquad \forall \zeta, \theta \in \text{the star}$$

We thus also satisfy the constraint $r_\zeta > 0$, which insures that r is a monotonically increasing function of ζ. In practice we shall set $R_i(\theta)$ surfaces to isobars.

With the above considerations, we adopt the following mapping

$$r(\zeta, \theta) \equiv r_i(\zeta, \theta) = \xi \Delta\eta_i + R_i(\theta) + A_i(\xi)(\Delta R_i(\theta) - \Delta\eta_i), \qquad \text{with} \qquad \xi \in [0, 1] \tag{37}$$

for the domain $\mathcal{D}_i$. From (37) we find

$$\begin{aligned} r_\zeta &= 1 + A_i'(\xi)\left(\frac{\Delta R_i(\theta)}{\Delta\eta_i} - 1\right) \\ r_\theta &= R_i'(\theta) + A_i(\xi)\Delta R_i'(\theta) \\ r_{\zeta\theta} &= A_i'(\xi)\frac{\Delta R_i(\theta)}{\Delta\eta_i} \\ r_{\zeta\zeta} &= \frac{A_i''(\xi)}{\Delta\eta_i}\left(\frac{\Delta R_i(\theta)}{\Delta\eta_i} - 1\right) \end{aligned}$$

where the primes indicate derivation.

The use of the (ζ, θ, φ) coordinates leads to new expressions of differential operators. We give a short account of their new form together with the metric tensor and the needed tensorial quantities in the appendix of the paper.

Finally, we should give the mapping in the outer empty domain surrounding the star. There, we choose the following expression:

$$r(\zeta, \theta) \equiv r_{\text{ex}}(\zeta, \theta) = \zeta - 1 + R_i(\theta) \qquad \text{with} \qquad \zeta \in [1, +\infty[\tag{38}$$

namely a linear mapping that smoothly continues the inner one in the last domain. The grid points are of course distributed using another mapping that connects the infinite domain to a finite one, namely

$$\zeta = \frac{1}{1 - \xi} \qquad \text{with} \qquad \xi \in [0, 1]$$

3.3. Interface conditions between domains

At the domain boundaries we need writing continuity conditions that link the fields in each domain. The main issue is that the mapping given by (37) has discontinuities in some of its derivatives. One easily finds that

$$r_\zeta(\eta_i) = 1, \qquad r_\theta(\eta_i) = R_i'(\theta), \qquad r_{\zeta\theta}(\eta_i) = 0$$

	Continuity between subdomains	
	Our mapping	The linear mapping
r	Yes	Yes
r_ζ	Yes	No
$r_{\zeta\zeta}$	No	Yes
r_θ	Yes	Yes
$r_{\theta\theta}$	Yes	Yes
$r_{\zeta\theta}$	Yes	No

Table 1: Continuity of the various derivatives at the interface between domains for the linear mapping (32) and our mapping.

so that all these quantities are continuous at the interfaces of the domains. On the contrary $r_{\zeta\zeta}$ is not continuous. We summarize these properties in Tab. 1 along with those of the linear mapping (32). Although simpler, the linear mapping has more discontinuities between domains.

In the case of a scalar field $\phi(r,\theta)$, if ϕ is continuous between subdomains, we simply need to impose

$$\phi^{(+)} = \phi^{(-)} \tag{39}$$

where $(+)$ and $(-)$ represent each side of the domains interfaces. If in addition we want ϕ to be derivable across the boundary, we have to write a condition on its normal derivative $\hat{\mathbf{n}} \cdot \nabla\phi$ (and not on $\frac{\partial\phi}{\partial\zeta}$), namely,

$$\hat{\mathbf{n}} \cdot \nabla^{(+)}\phi^{(+)} = \hat{\mathbf{n}} \cdot \nabla^{(-)}\phi^{(-)} \tag{40}$$

Noting that

$$\hat{\mathbf{n}} \cdot \nabla\phi = \sqrt{1 + \frac{r_\theta^2}{r^2}} \left(\frac{1}{r_\zeta} \frac{\partial\phi}{\partial\zeta} - \frac{r_\theta}{r^2 + r_\theta^2} \frac{\partial\phi}{\partial\theta} \right) \tag{41}$$

and that r, r_θ and $\partial_\theta\phi$ are continuous across the interface, which is a ζ = Cst surface, then condition (40) becomes

$$\frac{1}{r_\zeta^{(+)}} \left(\frac{\partial\phi}{\partial\zeta} \right)^{(+)} = \frac{1}{r_\zeta^{(-)}} \left(\frac{\partial\phi}{\partial\zeta} \right)^{(-)} \tag{42}$$

that is equivalent to saying $\left(\frac{\partial\phi}{\partial r} \right)^{(+)} = \left(\frac{\partial\phi}{\partial r} \right)^{(-)}$. Since our mapping ensures that $r_\zeta^{(+)} = r_\zeta^{(-)}$, we also have

$$\left(\frac{\partial\phi}{\partial\zeta} \right)^{(+)} = \left(\frac{\partial\phi}{\partial\zeta} \right)^{(-)} \tag{43}$$

In the case of a continuously differentiable vector field, the conditions of continuity of the

field are simply those of the components, namely

$$\begin{aligned} V^{\zeta(+)} &= V^{\zeta(-)} \\ V^{\theta(+)} &= V^{\theta(-)} \\ V^{\varphi(+)} &= V^{\varphi(-)} \end{aligned} \tag{44}$$

while the continuity of the normal derivative, namely $\hat{\mathbf{n}} \cdot \nabla \mathbf{V}$, leads to

$$\begin{aligned} \left(\frac{\partial V^{\zeta}}{\partial \zeta}\right)^{(+)} + \frac{1}{r_{\zeta}^{(+)}}\left(r_{\zeta\zeta}^{(+)} V^{\zeta(+)} + r_{\zeta\theta}^{(+)} V^{\theta(+)}\right) &= \left(\frac{\partial V^{\zeta}}{\partial \zeta}\right)^{(-)} + \frac{1}{r_{\zeta}^{(-)}}\left(r_{\zeta\zeta}^{(-)} V^{\zeta(-)} + r_{\zeta\theta}^{(-)} V^{\theta(-)}\right) \\ \frac{1}{r_{\zeta}^{(+)}}\left(\frac{\partial V^{\theta}}{\partial \zeta}\right)^{(+)} &= \frac{1}{r_{\zeta}^{(-)}}\left(\frac{\partial V^{\theta}}{\partial \zeta}\right)^{(-)} \\ \frac{1}{r_{\zeta}^{(+)}}\left(\frac{\partial V^{\varphi}}{\partial \zeta}\right)^{(+)} &= \frac{1}{r_{\zeta}^{(-)}}\left(\frac{\partial V^{\varphi}}{\partial \zeta}\right)^{(-)} \end{aligned} \tag{45}$$

which reduces to

$$\begin{aligned} \left(\frac{\partial V^{\zeta}}{\partial \zeta}\right)^{(+)} + \frac{r_{\zeta\zeta}^{(+)}}{r_{\zeta}^{(+)}} V^{\zeta(+)} &= \left(\frac{\partial V^{\zeta}}{\partial \zeta}\right)^{(-)} + \frac{r_{\zeta\zeta}^{(-)}}{r_{\zeta}^{(-)}} V^{\zeta(-)} \\ \left(\frac{\partial V^{\theta}}{\partial \zeta}\right)^{(+)} &= \left(\frac{\partial V^{\theta}}{\partial \zeta}\right)^{(-)} \\ \left(\frac{\partial V^{\varphi}}{\partial \zeta}\right)^{(+)} &= \left(\frac{\partial V^{\varphi}}{\partial \zeta}\right)^{(-)} \end{aligned} \tag{46}$$

for our mapping. These conditions are equivalent to saying that the viscous stress is continuous across the interface in case $\mathbf{V}$ is a velocity field. Note that this condition would be more complex with a linear mapping because r_{ζ} is not continuous in this latter case.

4. The discretization

As far as discretization of the differential operators is concerned, we chose a spectral grid in each domain. We thus use the Gauss-Lobatto grid for the radial coordinate ξ and the spherical harmonic expansion for the horizontal dependence. The identity of our spheroidal coordinates with spherical coordinates near the center insures the regularity of the radial functions at the origin[4]. Hereafter, N_r will refer to the number of points of the radial Gauss-Lobatto grid for the whole star, $\mathrm{L_{max}}$ will refer to the highest degree of spherical harmonics used in the solution and N_θ to number of grid points in latitude. Because of the imposed equatorial symmetry of the models, $\mathrm{L_{max}} \simeq 2N_\theta$.

The choice of a spectral representation is motivated by the precision of spectral methods at a given resolution (Canuto et al., 2007). Such precision is required when eigenmodes and eigenfrequencies of a star are computed and compared to observations. Previous computations

[4]We recall that a scalar function expanded over the spherical harmonics basis $f(r,\theta,\varphi) = \sum_{\ell,m} f_\ell^m(r) Y_\ell$ has radial components that verify $f_\ell^m(r) \sim r^\ell$ when $r \to 0$.

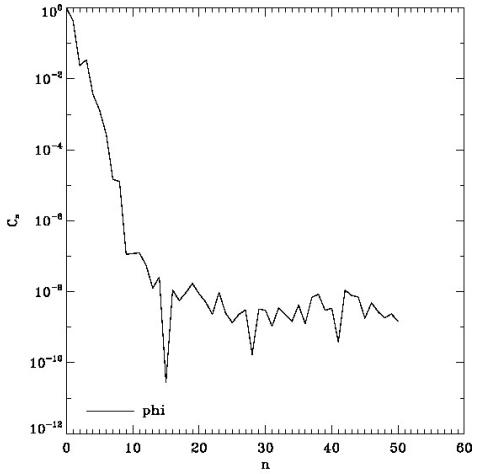

Figure 4: Spectrum of the gravitational potential from the solution of Poisson's equation for a n=3/2 polytrope. C_n represents the absolute value of the n$^{\text{th}}$-Chebyshev coefficient. The star is covered by a single domain.

of polytropic stars (see below) with finite-difference schemes have shown poor precision (e.g. Aksenov and Blinnikov, 1994). For a virial test (see below) to be met at a relative precision of 10^{-8}, finite-differences need 5000 radial points (Aksenov and Blinnikov, 1994), while the same problem with the same precision is solved with typically 20 points only when using the Gauss-Lobatto collocation grid (see Fig. 4). Our spectral method with domain decomposition is based on the strong formulation of the problem: equations or boundary/interface conditions are applied on given collocation points without any overlapping of the domains unlike the weak formulation (e.g. Canuto et al., 2007). As previously mentioned, the multidomain formulation turns out to be better adapted to the strong variations of ρ and provides more flexibility in the radial distribution of grid points (see Fig. 10).

Hence, the choice of a spectral element method turns out to be natural. We note that except relativistic stars (e.g. Bonazzola et al., 1998), stellar models have never been computed with a spectral method. All one-dimensional codes use finite-differences (like the MESA code of Paxton et al. 2011 or the TGEC code, e.g. Hui-Bon-Hoa 2008, etc.) except the CESAM code, which is based on splines (Morel, 1997; Morel and Lebreton, 2008).

5. The algorithm

The existence of a converging algorithm for such a nonlinear and complicated problem was the main uncertainty of the feasibility of this modeling. We explored two algorithms, namely Picard and Newton iteration schemes, which we shall now describe and discuss in the context of our problem.

5.1. Picard's iterative scheme

Picard's algorithm is known as a very intuitive scheme for solving iteratively nonlinear equation. It does only require the solving of a linear equation that is already present in the physical

problem at hands. As such, it has been employed in many different problems: flows in porous media (Paniconi and Putti, 1994), ice sheet flows (Lemieux et al., 2011), MHD equilibria in tokamaks (Oliver et al., 2006), and certainly many other problems. Although we finally left this method for Newton's one, as actually done by all the above mentioned works, it is worth mentioning the results we obtained with it, at least to assess its efficiency and its limits in our stellar modeling problem.

To present the results, we focus on the reduced problem of rigidly rotating *polytropic stars*. The general problem of modeling the steady state of rotating stars, as represented by equations (1)-(22), is strongly simplified when one assumes a polytropic equation of state instead of the general one[5], namely if we assume that the pressure only depends on the density through a power law like

$$P = K\rho^{1+1/n} \tag{47}$$

where K is a constant and n is the polytropic index. In such a case the star may rotate as a solid-body[6] and in the appropriate rotating frame, one just needs to solve the hydrostatic equation, namely

$$-\nabla P - \rho\nabla\Phi_{\text{eff}} = \mathbf{0} \tag{48}$$

where Φ_{eff} is the effective potential, namely the sum of the gravitational potential Φ and the centrifugal potential $-\frac{1}{2}\Omega^2 s^2$ (Ω is the angular velocity of the rigidly rotating polytrope). From (47) and (48), it is easy to derive the expression of density as a function of the gravitational potential. Using scaled variables, Poisson's equation can be rewritten as

$$\nabla^2\Phi = \left(1 - \Lambda(\Phi - \Phi_0) + \frac{1}{2}\Omega^2 s^2\right)^n = \rho(\Phi) \tag{49}$$

where $\Lambda = (1+\Omega^2/2)/(\Phi_{\text{eq}} - \Phi_c)$. In these expressions, Φ_{eq} and Φ_c are the equatorial and central values of the gravitational potential respectively.

For this "simple" problem, we used a mapping with only two domains: one for the star, the other for the surrounding vacuum (which we actually limit to a sphere of radius $2R_{\text{eq}}$). To use Picard's method we also rewrite the Poisson equation $\nabla^2\Phi = \rho(\Phi)$ as

$$\tilde{\nabla}^2\Phi = \frac{1}{g}\left(\rho(\Phi) + \text{NS}\right) + \left(1 - \frac{g^{\zeta\zeta}}{g}\right)\tilde{\nabla}^2\Phi \tag{50}$$

hence following Bonazzola et al. (1998). In this expression $\tilde{\nabla}^2$ represents the spherical part of the Laplacian operator, namely

$$\tilde{\nabla}^2 = \frac{\partial^2}{\partial\zeta^2} + \frac{2}{\zeta}\frac{\partial}{\partial\zeta} + \frac{\Delta_{\theta\varphi}}{\zeta^2} \qquad \text{with} \qquad \Delta_{\theta\varphi} = \frac{1}{\sin\theta}\frac{\partial}{\partial\theta}\sin\theta\frac{\partial}{\partial\theta} + \frac{1}{\sin^2\theta}\frac{\partial^2}{\partial\varphi^2},$$

[5]Polytropic stellar models are a valid option for fully convective stars (i.e. stars with a mass less than 0.6 solar mass) and for low-mass white dwarf stars for which the polytropic index is 3/2. Due to their simplicity, these models have been the first to be computed in two dimensions (e.g. James, 1964).

[6]Non-uniform rotation of polytropic stars have been explored by Eriguchi and Müller (1985), Aksenov and Blinnikov (1994) and MacGregor et al. (2007).

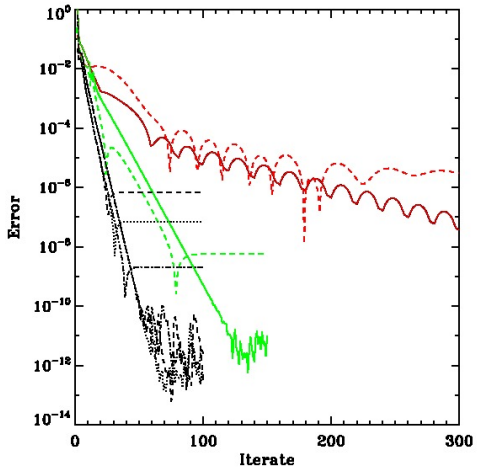

Figure 5: Convergence of the Picard iterations for the solution of the rotating n=3/2-polytropic star. Black curves show the errors ε_1 and ε_2 of (51) and (52) as a function of the iteration number for different spatial resolution in the $\Omega = 0.5$ case: dashed line $L_{\max} = 8$ and Nr=32, dotted line $L_{\max} = 16$ and Nr=32, dashed-dotted line $L_{\max} = 32$ and Nr=64. The curves terminating by an horizontal plateau show the ε_2-virial test. The two red curves show the ε_1 (solid) and ε_2 (dashed) errors for a case near criticality ($\Omega = 0.77$ see table 2) and with resolution $L_{\max} = 64$ and Nr=128. The two green curves show the same case as the red one, but when the grid is frozen at some stage of the iterations.

and "NS" represents the non-spherical terms that, together with $\tilde{\nabla}^2$, form the expression of the Laplacian in spheroidal geometry. $g = \max(g^{\zeta\zeta})$ over each domain[7]. $g^{\zeta\zeta}$ is a component of the metric tensor (see appendix).

With Picard iterative scheme, equation (50) is solved in the following way for the N+1$^{\text{th}}$-iterate

$$\tilde{\nabla}^2\Phi_{N+1} = \frac{1}{g_N}\,(\mathrm{NS}+\rho)_N + \left(1-\frac{g^{\zeta\zeta}}{g}\right)_N \left(\lambda(\tilde{\nabla}^2\Phi)_N + (1-\lambda)(\tilde{\nabla}^2\Phi)_{N-1}\right)$$

where λ is a relaxation parameter usually set to 0.5 (but 1 is found to work better here).

In Fig. 5, we show the convergence rate of the iterations towards the solution for various spectral resolutions and for two rotation rates, in the case of a polytropic index equal to 3/2.

To appreciate the convergence and the precision of the solution, we examine two quantities: first the relative error on the gravitational potential as a whole, namely

$$\varepsilon_1 = \frac{\max_{\text{star}}(|\Phi_N - \Phi_{N-1}|)}{\max_{\text{star}}(|\Phi_N|)} \tag{51}$$

second, the error on the virial equality. Indeed, from the momentum equation it can be shown that the exact solution must satisfy the virial equality:

[7]The use of the global maximum value is not recommended as we experienced a better convergence when the maximum is evaluated on each subdomain.

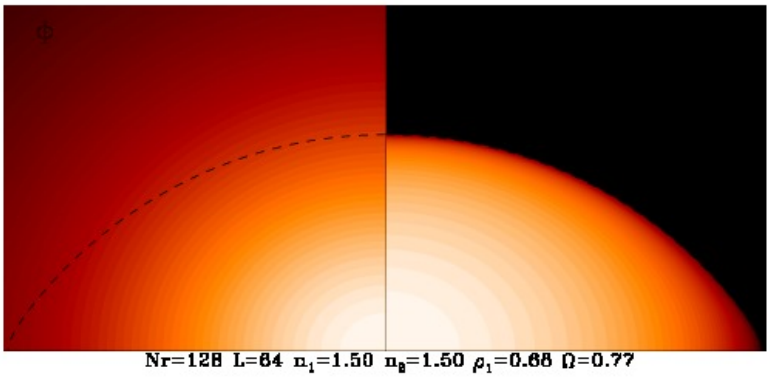

Figure 6: Distribution of the gravitational potential (left) and density (right) for a n=3/2-polytropic star rotating near criticality $\Omega/\Omega_{\rm crit} \simeq 0.98$. The ratio of the equatorial and polar radii is $R_{\rm eq}/R_{\rm pol} = 1.58$, corresponding to a flatness of $\varepsilon = 0.367$.

$$I\Omega^2 + W + 3P = 0$$

where Ω is the angular velocity of the polytrope, and

$$I = \int_{(V)} r^2 \sin^2\theta \rho dV, \qquad W = \frac{1}{2}\int_{(V)} \Phi\rho dV, \qquad P = \int_{(V)} pdV$$

which represent physically the inertia moment, the gravitational binding energy and the internal energy respectively. The quantity

$$\varepsilon_2 = 1 + \frac{I\Omega^2 + 3P}{W} \tag{52}$$

therefore measures the quality of the solution and incorporates the three types of errors that plague the numerical solution: (i) the truncation (spectral) error, iteration error and round-off errors.

Let us now discuss the results. For the first rotation rate, $\Omega = 0.5$ in our units, which corresponds to a configuration rotating at 68% of the critical angular velocity $\Omega_c = \sqrt{GM/R_{\rm eq}^3}$ and a flatness[8] of 0.18, Fig. 5 shows that the convergence of the solution is rather fast. We observe that whatever the spectral resolution, Φ converges exponentially and reaches the round-off error after ~ 50 iterations. The level of numerical noise is likely the results of the way the nonlinear terms are computed and depends also on the condition number of the linear operator. Quite remarkably, this effect depends very little on the spatial resolution.

[8]The flatness is defined as the ratio $(R_{\rm eq} - R_{\rm pol})/R_{\rm eq}$. It measures the relative extension of the equatorial radius compared to the polar one.

The virial error, is also sensitive to the spectral trunction. Thus it first decreases as the error on the fields and then converges to the spectral error. When spectral resolution is increased, this error is decreased as expected.

The foregoing rotation rate ($\Omega = 0.5$) represents rather fast rotating stars, but some stars rotate near criticality. To test the efficiency of the method we therefore set the rotation rate to $\Omega = 0.77$, which leads to a configuration that rotates at 98% of the critical angular velocity. As shown by Fig. 6, at this angular velocity the radius of curvature of the surface at equator is quite small. Actually, at critical angular velocity, the star develops an equatorial cusp, namely a non-smooth, discontinuous, variation of the North-South tangent vector. This implies that stellar models rotating near criticality are very demanding in angular resolution, and thus in the spherical harmonic expansion. As shown in Fig. 5 (red pluses), convergence is now very slow. Actually, the algorithm does not converge if a high precision on the solution is required. A high precision solution at rotation rates close to criticality can nevertheless be achieved (see table 2), by decoupling the iterations on the grid from those on matter distribution. This is indeed possible in the case of a polytropic star, since we are solving for the gravitational potential, whose boundary conditions are set at the star center and at infinity. Hence, even if the interface between the domains does not match perfectly the true surface of the star, this has little influence on the precision of the solution. Thus, when computing the $\Omega/\Omega_c = 0.99$ solution of table 2, we freezed the grid evolution when its flatness exceeds 30%, otherwise matter distribution slighly oscillates with the grid[9]. We note that a similar trick has been used by Gourgoulhon et al. (2001) for modeling binary stars. In table 3, we show similar results for the n=3-polytrope. We note that a much lower radial resolution is needed to reach the required precision than with the n=3/2-polytrope. The reason for that comes from the differentiability of the density near the surface since $\rho \sim (R(\theta) - r)^n$ there. The high n polytropes are more easily represented with Chebyshev polynomials than the low n's (see Bonazzola et al., 1998, for a thorough discussion of this point).

5.2. Newton's iterative scheme

5.2.1. Implementation

Newton's algorithm solves iteratively a set of nonlinear equation $\mathbf{F}(\mathbf{X}) = \mathbf{0}$ by assuming that a trial solution is close to the actual solution so that a first order expansion of $\mathbf{F}(\mathbf{X})$ can be used. If $\mathbf{X}_N$ is the N^{th} iterate then the correction $\delta\mathbf{X}$ towards the true solution is obtained through

$$\mathbf{F}(\mathbf{X}_N + \delta\mathbf{X}) = \mathbf{0} \implies [J]\delta\mathbf{X} = -\mathbf{F}(\mathbf{X}_N)$$

where $[J]$ is the Jacobian matrix of the nonlinear operator.

We first tested Newton's method on the polytropic star without rotation, thus in a one-dimensional situation to assess the good behaviour of the scheme. We show the result in Fig. 7 along with the result obtained with Picard iterations. Newton's method nicely works and offers a fast (quadratic) convergence rate as expected.

The specificity of our problem is that the grid is changing with the iterations and therefore the mapping described in Sect. 3 is also part of the variational problem that defines the Jacobian. More precisely, the boundaries of the domains are part of the vector $\mathbf{X}$ defining the solution. Hence, differential operators, which always use the metric tensor, should also be differentiated with respect to the grid variation. For instance, the functional variation of the radial distance in the i^{th}-domain is given by

[9] Other alternatives, like the use of a relaxation parameter, are possible, but our trick turned out to be more expeditious.

					Picard		Newton	
Ω	Ω/Ω_c	ε	L	N_r	N_{iter}	CPU (s)	N_{iter}	CPU (s)
0.3	0.38	0.073	8	80+25	36	2	15	2
0.5	0.64	0.183	14	90+25	40	3	21	4.2
0.6	0.77	0.248	22	90+25	60	6	23	7.9
0.7	0.90	0.317	42	90+25	137	23	25	31
0.74	0.95	0.346	70	80+25	138	38	27	92
0.76	0.98	0.361	120	90+25	158	87	27	600
0.772	0.99	0.370	200	210+31	120	373		

Table 2: Characterization of the efficiency of the Picard and Newton iterations for the computation of a n=3/2-polytrope at increasing rotation rates. Ω/Ω_c gives the (uniform) angular velocity in terms of the critical angular velocity and ε is the flatness of the rigidly rotating polytropic star. L, N_r and N_{iter} are the minimum angular, radial resolutions and number of iteration to reach a virial test less than 10^{-9}. CPU gives the CPU time in seconds needed for the execution of the gfortran-compiled code on an Intel Core i5-5200U CPU @ 2.20GHz. The last row at extreme rotation needed a slight change in the Picard algorithm (see text), hence the lower number of iterations. For Newton iterations we first start with the computation of a 1D-model and continue with the desired 2D-model. We only give the number of iterations needed by the 2D solutions, since they are the slowest.

$$\delta r^i = (\xi - A_i(\xi))\delta\Delta\eta_i + \delta R_i(\theta) + A_i(\xi)\delta\Delta R_i(\theta)\ ,$$

its ζ-derivative by

$$\delta r^i_\zeta = A_i'(\xi)\left(\frac{\delta\Delta R_i(\theta)}{\Delta\eta_i} - \frac{\Delta R_i(\theta)}{\Delta\eta_i^2}\delta\Delta\eta_i\right)$$

etc. These variations impact the variational form of the partial differential equations. For instance, Poisson's equation yields

$$\Delta\delta\phi + (\delta\Delta)\phi = \delta\pi_c\rho + \pi_c\delta\rho$$

In this expression $\delta\Delta$ means the variation on the Laplacian operator induced by the variation on the mapping. More explicitly, from (A.57), we find that

$$\delta\Delta = \delta g^{\zeta\zeta}\frac{\partial^2}{\partial\zeta^2} + \cdots \qquad \text{with} \qquad \delta g^{\zeta\zeta} = 2\frac{r\delta r + r_\theta\delta r_\theta}{r^2 r_\theta^2} - 2g^{\zeta\zeta}\frac{r_\zeta\delta r + r\delta r_\zeta}{r r_\zeta}$$

Hence, the expression of the Jacobian matrix is particularly cumbersome.

Once the Jacobian matrix is evaluated the linear system needs to be solved. Typical resolutions need 300 grid points in the radial direction and 24 points in latitude (the star is assumed

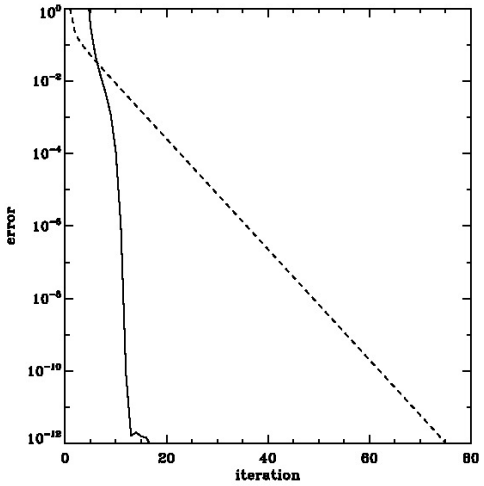

Figure 7: Convergence of Picard iterations (dashed line) and Newton iterations (solid line) towards the solution of a non-rotating polytropic star for n=3.5, using 100 radial grid points on a Gauss-Lobatto grid.

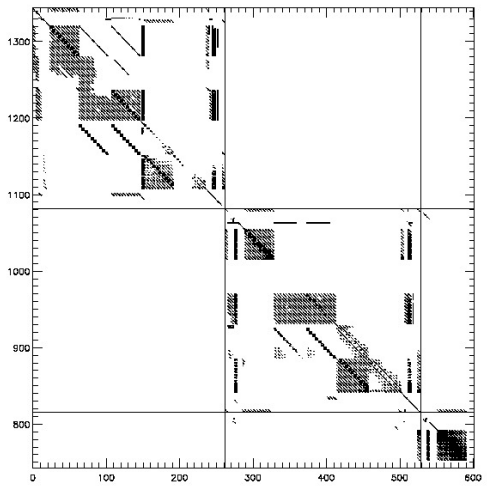

Figure 8: Shape of the Jacobian matrix (only first blocks shown). Grey and black dots show non-zero elements while vertical and horizontal lines delineate the position of the blocks. For this case $N_\theta = 4$, $N_r = 10$ per domain.

					Picard		Newton	
Ω	Ω/Ω_c	ε	L	N_r	N_{iter}	CPU (s)	N_{iter}	CPU (s)
0.2	0.44	0.069	8	28+13	50	0.5	9	1
0.3	0.66	0.151	14	28+15	64	1	13	1.3
0.35	0.77	0.203	20	28+17	75	1.2	14	1.5
0.41	0.90	0.275	48	28+19	136	6	16	4.2
0.43	0.95	0.302	80	28+19	130	13	17	10.8
0.445	0.98	0.323	176	32+25	120	78	20	145
0.45	0.99	0.330	200	32+25	140	127	20	187

Table 3: Same as in table 2 but for a n=3-polytrope.

equatorially symmetric). Thus, each physical scalar field generates a vector of about 10^4 components so that the needed five scalar fields together form a vector of few 10^4, thus a rather large, full matrix.

We solve this problem by a combination of a direct LU-solver and the iterative Conjugate Gradient Squared (CGS) method (Sonneveld, 1989). Schematically, when the star is divided into shell-like domains, the Jacobian matrix has a banded structure actually made of coupled blocks of size determined by the resolution (see Fig. 8). Since the CGS method needs preconditioning to be efficient, we first LU-factorize the whole matrix taking advantage of its tri-diagonal block structure. We thus generate a split pre-conditionner for the CGS solver. However, the LU-factorization is expensive in terms of CPU time so that the pre-conditionner is updated only when CGS iterations do not converge within some fraction of the LU-factorization time. A similar kind of algorithm has been used by Einset and Jensen (1992) to solve 3D mixed convection flows. Our algorithm may be summarized as follows:

1. Read the initial model or build it (only in 1D)
2. Build the Jacobian matrix
3. LU-factorize the Jacobian matrix
4. CGS-solve for the correction $\delta\mathbf{X}$
5. Update $\mathbf{X}$
6. Recompute the RHS and the Jacobian matrix
7. Attempt another CGS solution to derive the new $\delta\mathbf{X}$ using the former LU matrices as a preconditionner. Namely, if L_k and U_k are the factors of the Jacobian $\mathcal{J}_k$, the $k+1$ equation is solved with the (split-preconditioned) CGS solver as

$$J_k^{k+1} U_k \delta\mathbf{X}_{k+1} = -L_k^{-1}\mathbf{F}_{k+1}$$

   where $J_k^{k+1} = L_k^{-1}\mathcal{J}_{k+1}U_k^{-1}$ is the preconditionned matrix. If the convergence of this iterative method is less than say N iterates, then the algorithm continues at step 5. N is chosen such that the N iterations are faster than a LU factorization. If convergence is not reached, then the algorithm continues on step 3
8. if $||\delta\mathbf{X}||/||\mathbf{X}|| \leq$tolerance, then stop.

5.2.2. Test on the two-dimensional polytrope

Since Picard method gives good results on the rotating 2D polytrope, this problem offers a good set of comparisons for the methods.

When the iterations are started from scratch, Newton's scheme is much slower than Picard's. The reason for that is the huge size of the Jacobian matrix compared to the block-diagonal matrix of the Picard iteration. Thus even if Newton's scheme uses much less iterations, their cost immediately ruins its efficiency. Fortunately, Newton's scheme can be easily improved if it first computes a 1D-model and use this model as a start of the 2D-model. This much reduces the total CPU times and Newton's method is then competitive.

The number of iterations and the needed CPU time for Newton's method are given in tables 2 and 3. From these results we observe that Picard and Newton methods have a similar efficiency when the rotation rate is less than the 90% of the critical one. Beyond this value, the required angular resolution is large and Newton scheme has to deal with large full matrices which strongly slow down the calculation. Hence, for the simple polytropic stars and for the ultimate rotation rates, Picard's method appears to be the most efficient[10].

6. Numerical solution of stellar models

We now turn to realistic stellar models as the one shown in Fig. 1 or 2 and present their numerical characteristics. Unless otherwise stated, we consider a 5 $M_\odot$ stellar model, with a chemically homogeneous composition close to the solar one (X=0.7, Y=0.28 and Z=0.02). Such a model would describe a zero-age main sequence B-star of our Galaxy.

6.1. Picard's method

The foregoing results let us think that Picard method should also work with the complete set of equations (24 – 25). Unfortunately, this has not been the case. Using Kramers type opacities (power laws) together with a simple equation of state (ideal gas), we could not reach convergence when the angular velocity reached values above $\Omega \sim 0.35\Omega_c$. We ascribed this failure to the bad conditioning of the linear operator, which now includes new coupling terms, the worst of them coming from the momentum equation.

In view of the foregoing failure, we tried Newton's scheme on this problem. We shall now present the results of this successful attempt.

6.2. One-dimensional models with Newton's scheme

As is well-known, Newton iterations show quadratic convergence when the initial guess is close enough to the actual solution. For our problem, this implies that 2D models need to be initiated by a non-rotating configuration of similar parameters just as for polytropes. We show in Fig. 9 the evolution of the relative L_2-norm $||\delta\mathbf{X}||/||\mathbf{X}||$ of Newton's corrections with the iteration number in the 1D and 2D cases. Since 1D iterations are extremely fast, they are started from 'scratch' and are hence wandering around (typically for 50 iterations) before the quadratic convergence operates. The whole computation takes a few seconds on a laptop computer. The result is then used to compute a 2D-model with $\Omega/\Omega_c = 0.66$ (resulting in a flatness of 0.181),

[10] To be fair with Newton scheme, a further split of the stellar domain into several subdomains may strongly accelerate the iterations, at the price of some loss of precision of course.

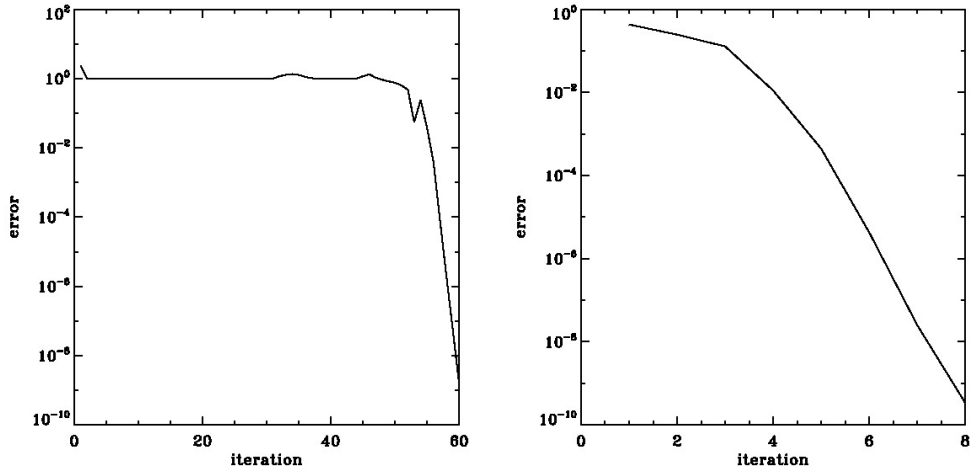

Figure 9: Left: Convergence of Newton's iterations for a 1D stellar model started from scratch (5 $M_\odot$ with homogeneous chemical composition - see text). Right: Convergence of Newton's iterations for a 2D model started from the converged 1D-model on left when $\Omega/\Omega_c = 0.66$.

which shows a very good convergence (e.g. Fig. 9 right), showing that a converged 1D model is an appropriate starting point for the computation of an already fast rotating model.

Before discussing 2D-models, we shall first focus on the numerical properties of the 1D models. Such models are indeed the first stellar models ever produced using spectral methods.

In Fig. 10 (top), we show the Chebyshev spectra, scaled by the coefficient of the zeroth order polynomial, for each domain used to compute the previous $5M_\odot$ 1D-model. The amplitude of the last coefficient gives the relative spectral error (or truncation error) of the Chebyshev polynomial representation. In such a realistic model, the equation of state and the opacities are computed from interpolated tables (OPAL). The spectral precision reflects the smoothness of the interpolated functions and is clearly limited to 10^{-6}. An increased spectral resolution does not much improve the precision. Very precise models are obtained when tabulated equation of state (EOS) and tabulated opacities are replaced by -less realistic- analytical formulae. For instance in Fig. 10 (middle) we use the ideal gas EOS and Kramers opacity laws (as in Espinosa Lara and Rieutord, 2007), namely

$$P = \mathcal{R}_* \rho T \qquad \text{and} \qquad \kappa = \kappa_0 \rho^a T^b \tag{53}$$

The solutions are then strikingly precise. We may also notice that the central domain owns a better precision than the other domains. The reason is that the central domain describes the convective core of the star. As discussed in section 2.1.3, we assume a constant entropy in stellar cores. Thus, numerical noise coming from opacity disappears and we recover a better convergence similar to the case of the polytrope (e.g. Fig. 4). It is not as good as the one obtained with (53) since the EOS remains more complex than that of the ideal gas.

The better convergence in the central core allows us to use less radial grid points there and to transfer them in the other domains. The precision of the global solution can thus be improved as shown in Fig. 10 (bottom). In this same figure we also tested Houdek and Rogl (1996) smooth

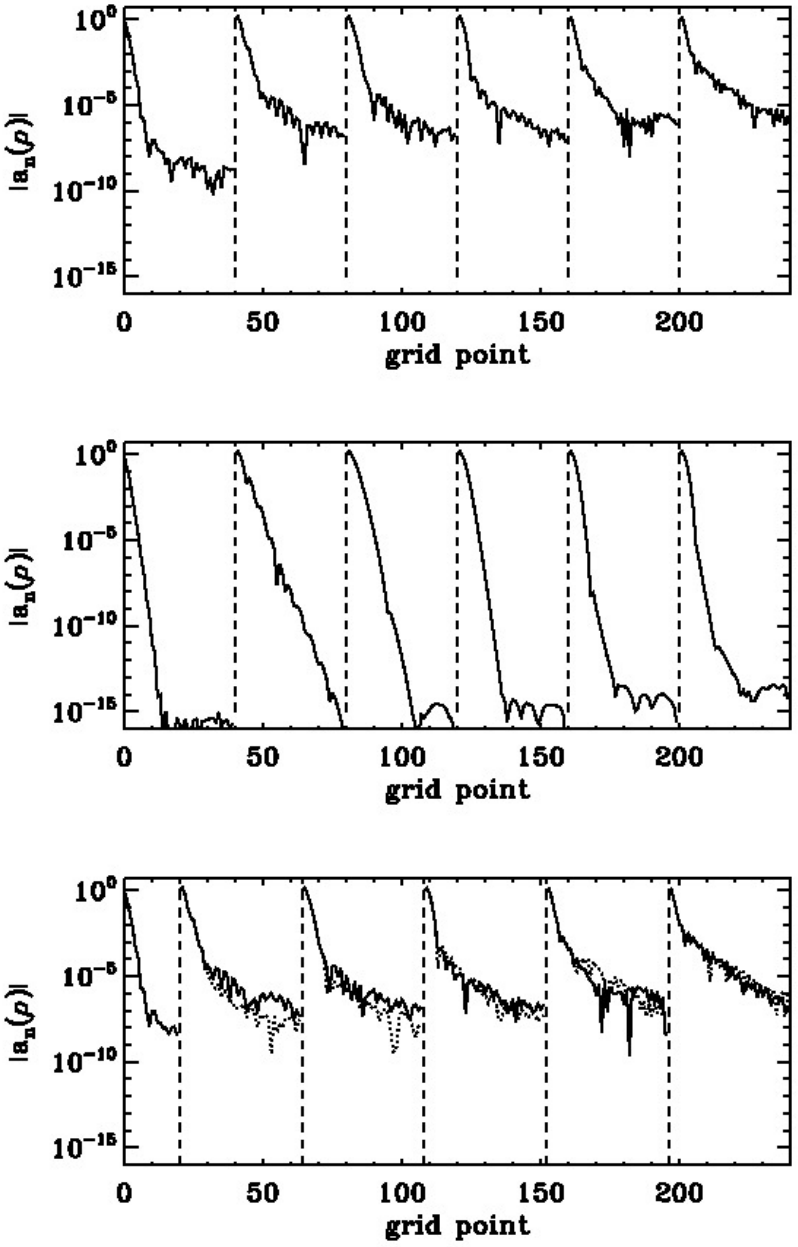

Figure 10: Top: Chebyshev spectrum in each domain for the density ρ of a 1D-stellar model of $5M_{\odot}$. We use 6 domains with 40 grid points each. Middle: similar model but where the equation of state is that of the ideal gas and where the analytic Kramers type opacities expressions are used. Bottom: Same as top but with a different distribution of grid points: 20 points in the first domain (convective core) and 44 in the remaining ones. The spectral precision of the solution is typically increased by an order of magnitude (see sect.6). The dotted lines show the spectra when Houdek & Rogl's interpolations of OPAL opacities are used (Houdek and Rogl, 1996).

Ω/Ω_c	ε	N_θ	N_r	$N_{\rm iter}$	CPU Time (s)	Precision
0.70	0.200	16	6×40	8	170	$10^{-8}, 7\times10^{-4}$
0.77	0.232	20	6×40	9	316	$2\times10^{-8}, 6\times10^{-4}$
0.90	0.294	24	6×40	+9	+423	$4\times10^{-8}, 6\times10^{-4}$
0.95	0.320	40	6×40	+9	+1200	$5\times10^{-8}, 3\times10^{-4}$
0.98	0.337	40	6×40	+11	+1260	$4\times10^{-7}, 4\times10^{-4}$
0.98	0.337	60	6×40	+9	+2150	$3\times10^{-8}, 5\times10^{-4}$
0.77	0.233	20	10×24	10	203	$2\times10^{-8}, 9\times10^{-4}$
0.90	0.295	24	10×24	+9	+217	$4.5\times10^{-8}, 7\times10^{-4}$
0.90	0.295	24	10×24	13	456	$4.5\times10^{-8}, 7\times10^{-4}$

Table 4: Some data showing the numerical efficiency of the ESTER code at computing 5 $M_\odot$ stellar models with fast rotation. Ω/Ω_c is the fraction of critical angular velocity at equator. ε is the flattening of the solution. N_θ is the number of grid points in latitude and N_r the number of grid points inside the star in the ζ-coordinate. N_r is given as the product of the number of domains times the number of points inside a domain (here all domains have the same resolution). CPU (s) gives the CPU-time needed for a run with a i5-4570 processor at 3.2GHz. Precision gives the numbers corresponding to the virial and energy tests (see text).*Upper part:* The $\Omega/\Omega_c = 0.7$ and $\Omega/\Omega_c = 0.77$ models are calculated from a 1D model, while the following models (with $\Omega/\Omega_c \geq 0.90$) are computed from the preceding one. Hence, the 0.90-model is iterated from the 0.77-model and needs 9-iterations using an additional 423s CPU time. The 0.95-model is computed from the 0.90-model with 9 additional iterations, etc. The 0.98-model was also computed with enhanced resolution ($N_\theta = 60$) from the 0.95-model. *Lower part:* Keeping the same number of radial grid points, the number of domain is increased to 10. A direct calculation of the 0.90-model is compared to a two-step calculation using an intermediate 0.77-model.

interpolations of OPAL tables, but as shown, the convergence is only slightly better in the central layers.

6.3. General properties of two-dimensional models

Two-dimensional models are all computed from similar (in mass and chemical composition) 1D-non-rotating models. We recall that 2D models need very few input parameters, namely, the mass, the equatorial angular velocity scaled by the keplerian one (i.e. $\Omega_{\rm eq}/\Omega_k$), the hydrogen mass fraction in the envelope (X), in the core (X_c), and the metallicity Z. Other parameters specify the numerical grid. Thus, compared to 1D model, we just need to specify the equatorial rotation rate or, equivalently, the total angular momentum.

From non-rotating models we can rather easily compute a model rotating at 77% of the critical angular velocity as shown in Tab. 4. For a model, rotating at 90% of the critical velocity this is still possible but the number of domains needs to be adjusted. Tab. 4 shows two examples of a computation of the 90%-case: one directly from the non-rotating model and the second with a first step at the 77%-case. The two-step calculation is slightly faster since the first steps can be done with less angular resolution.

In Tab. 4 we also give the accuracy of the solutions. For that, we use the virial test as previously explained (but see also Rieutord and Espinosa Lara, 2013) and the energy test which

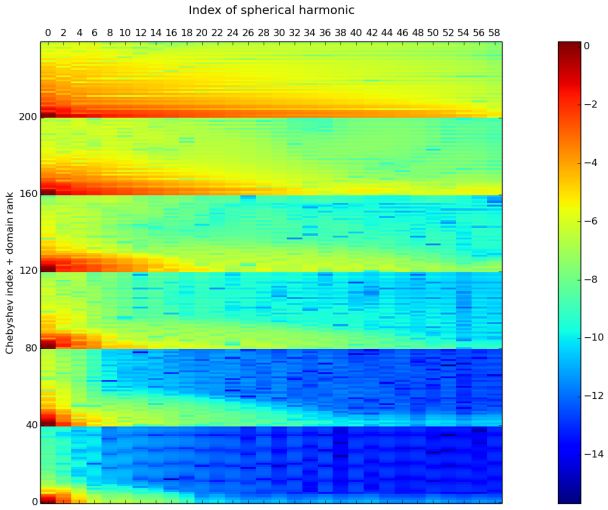

Figure 11: 2D spectra of the density showing the convergence of the solutions both in the spherical harmonic basis (horizontal axis) and in the radial direction (vertical axis). In the radial direction, each domain owns 40 grid points that give 40 Chebyshev coefficients (the color scale is logarithmic). For this plot we used a 5 $M_\odot$ model rotating at 95% of the critical angular velocity.

demands that

$$\int_{(S)} \chi \nabla T \cdot d\mathbf{S} + \int_{(V)} \varepsilon_* dV = 0 \, . \tag{54}$$

This latter test expresses the conservation of energy. The results given in Tab. 4 clearly show that this is satisfied to a lower precision than the virial test. This is again an effect of the actual numerical accuracy of the OPAL tables for opacity.

2D solutions must also satisfy spectral convergence in the horizontal direction, namely on the spherical harmonic basis. In Fig. 11, we show a view of the corresponding 2D-spectrum. Since the stellar domain is divided into six "radial" domains, we get six 2D-spectra. Putting them side by side, we can appreciate the changes of the convergence with the position of the domain in the star. As in the 1D-case, surface layers are the most difficult for spectral convergence. In these layers two effects combine: the rapid variations of opacity and the more flattened shape of outer domains compared with inner ones. This latter effect impacts on the needed number of spherical harmonics.

6.4. Numerical performances

In the present version of the algorithm, the resolution of the linear system associated with each Newton iteration is made through an LU factorization and CGS iterations. The left and right preconditionning matrices needed by the CGS algorithm are obtained from the LU factorization of the Jacobian. This is an efficient preconditioning since it allows convergence with 2 or 3

CGS iterations. However, the LU factorization is an expensive operation whose cost grows as n^3 compared to the matrix-vector products, or back substitutions, that are used by the CGS scheme and which scale as n^2 (n is the size of the blocks). Thus, if N_d is the number of domains, N_r the total number of radial grid points, and N_θ the number of latitude grid points, the number of flops for each Newton iteration increases as $N_r^3 \times N_\theta^3/N_d^2$, since the LU factorization dominates the costs. This expression readily shows that increasing the number of domains is computationnaly advantageous. However, this is at the expense of radial spectral precision (assuming that the total number of radial grid points is fixed).

Actually, the optimal number of domains is such that radial and horizontal spectral precision are about the same, which means that the number of grid point per domain should be $\sim N_\theta^2$. Table 4 shows that models calculations are affordable on a desktop/laptop computer for models rotating up to 98% of the critical angular velocity. Beyond this value, the needed angular resolution gets very large because the stellar surface tends to be singular (see Fig. 6 and sect. 5.1). A cusp forms at the equator and other numerical techniques need to be considered.

7. Conclusions and outlooks

In this paper, we presented the computational techniques of the ESTER code, which computes the first stellar models based on spectral methods and which can address the two-dimensional case needed for fast rotating stars.

The first key feature of the ESTER models is their use of a coordinate system that is adapted to the shape of the star so that boundary conditions can be easily imposed at the stellar surface. This is dealt with a nonlinear mapping such that the new coordinate system reduces to the spherical coordinates in the neighbourhood of the star's center. This feature guarantees the regular behaviour of the radial spectral functions at the origin.

A second key feature of these models is that they use shell domains with a spectral decomposition inside each domain. Such a discretization of the partial differential equations benefits from the high precision of spectral methods and from the flexibility of domain distribution. This discretization belongs to the class of spectral element methods (Canuto et al., 2007).

The third key feature of the models is the choice of the algorithm for the iterative method solving the nonlinear partial differential equations of the problem. Both Picard and Newton schemes have been tested. The Picard algorithm turns out to be very efficient on the simple polytropic models of stars but loses its efficiency in stellar models with more complex physics. On the contrary, Newton algorithm does not performs very well with simple polytropes (in term of computing time), but is unsurpassed on realistic stellar models with a complex microphysics (including tabulated data).

The last key feature of our models is the combined use of LU factorization and CGS iterations for the solving of Newton's iterations. The CGS algorithm is crucial when 2D solutions are computed. It makes these solutions affordable on small computers and does not jeopardize future improvements including more complex physics.

This last point brings us to the possible and necessary future developments of the ESTER code. These will have to deal with time evolution. But stellar evolution is a long timescale process and therefore short timescale motion like turbulence, should still be replaced by a mean-field modeling. Present 1D models solve stellar evolution by chaining hydrostatic models in a Lagrangian framework. Thus, modeling stellar evolution requires the computation of thousands of models. In the two-dimensional framework, the flows and the changing shape of the star calls

for a mixt of the Lagrangian and Eulerian formalism. The numerous models that will have to be computed also demand that the numerical schemes are optimal. In this respect, improving the parallelism of the code will be crucial. The incomplete LU factorization is an interesting option for replacing the present LU factorization which has not a great scalability. A more challenging evolution of the code may be the use of Jacobian-free Newton-Krylov methods which avoids the arduous work of deriving the equations for the Newton corrections. However, for these methods, preconditioning is also a strong issue (Knoll and Keyes, 2004), and numerical efficiency is not guaranteed. Thus, time-evolution will also require some exploration to delineate the most appropriate numerical scheme, which is presently unknown.

Acknowledgements

We are very grateful to our colleague Daniel Reese for letting us use his (very) illustrative figure (3), and to the referee for very detailed and constructive remarks. The authors acknowledge the support of the French Agence Nationale de la Recherche (ANR), under grant ESTER (ANR-09-BLAN-0140). This work was also financially supported by the Centre National de la Recherche Scientifique through the Programme National de Physique Stellaire (PNPS, CNRS/INSU). The numerical calculations have been carried out using HPC resources from CALMIP (Grant 2015-P0107).

References

Aksenov, A. G., Blinnikov, S. I., Oct. 1994. A Newton iteration method for obtaining equilibria of rapidly rotating stars. A&A 290, 674–681.

Angulo, C., Arnould, M., Rayet, M., Descouvemont, P., Baye, D., Leclercq-Willain, C., Coc, A., Barhoumi, S., Aguer, P., Rolfs, C., Kunz, R., Hammer, J. W., Mayer, A., Paradellis, T., Kossionides, S., Chronidou, C., Spyrou, K., degl'Innocenti, S., Fiorentini, G., Ricci, B., Zavatarelli, S., Providencia, C., Wolters, H., Soares, J., Grama, C., Rahighi, J., Shotter, A., Lamehi Rachti, M., Aug. 1999. A compilation of charged-particle induced thermonuclear reaction rates. Nuclear Physics A 656, 3–183.

Bonazzola, S., Gourgoulhon, E., Marck, J.-A., 1998. Numerical approach for high precision 3d relativistic star models. Phys. Rev. D 58, 104020.

Brott, I., Evans, C. J., Hunter, I., de Koter, A., Langer, N., Dufton, P. L., Cantiello, M., Trundle, C., Lennon, D. J., de Mink, S. E., Yoon, S.-C., Anders, P., Jun. 2011. Rotating massive main-sequence stars. II. Simulating a population of LMC early B-type stars as a test of rotational mixing. A&A 530, A116.

Busse, F., 1981. Do eddington-sweet circulations exist ? Geophys. Astrophys. Fluid Dyn. 17, 215.

Canuto, C., Hussaini, M. Y., Quarteroni, A., Zang, T. A., 2007. Spectral Methods Evolution to Complex Geometries and Applications to Fluid Dynamics. Springer Verlag.

Clement, M. J., Dec. 1974. On the solution of Poisson's equation for rapidly rotating stars. ApJ 194, 709–714.

Clement, M. J., Jun. 1978. On the solution of the equilibrium equations for rapidly rotating stars. ApJ 222, 967–975.

Clement, M. J., May 1979. On the equilibrium and secular instability of rapidly rotating stars. ApJ 230, 230–242.

Clement, M. J., Jan. 1994. Differential rotation and the convective core mass of upper main-sequence stars. ApJ 420, 797–802.

Deupree, R. G., Jul. 2011. Structure of Uniformly Rotating Stars. ApJ 735, 69.

Deupree, R. G., Castañeda, D., Peña, F., Short, C. I., Jul. 2012. Matching the Spectral Energy Distribution and P-mode Oscillation Frequencies of the Rapidly Rotating Delta Scuti Star α Ophiuchi with a Two-dimensional Rotating Stellar Model. ApJ 753, 20.

Domiciano de Souza, A., Kervella, P., Jankov, S., Abe, L., Vakili, F., di Folco, E., Paresce, F., Aug. 2003. The spinning-top Be star Achernar from VLTI-VINCI. A&A 407, L47–L50.

Einset, E. O., Jensen, K. F., 1992. A finite element solutionof three-dimensional mixed convection gas flows in horizontal chnnels using preconditioned iterative metrix methods. International Journal for Numerical Methods in Fluids 14, 817–841.

Eriguchi, Y., Müller, E., May 1985. A general computational method for obtaining equilibria of self-gravitating and rotating gases. A&A 146, 260–268.

Eriguchi, Y., Müller, E., Aug. 1991. Structure of rapidly rotating axisymmetric stars. I - A numerical method for stellar structure and meridional circulation. A&A 248, 435–447.
Espinosa Lara, F., Rieutord, M., 2007. The dynamics of a fully radiative rapidly rotating star enclosed within a spherical box. A&A 470, 1013–1022.
Espinosa Lara, F., Rieutord, M., 2013. Self-consistent 2D models of fast rotating early-type stars. A&A 552, A35.
Gourgoulhon, E., Grandclément, P., Taniguchi, K., Marck, J.-A., Bonazzola, S., 2001. Quasiequilibrium sequences of synchronized and irrotational binary neutron stars in general relativity: Method and tests. Phys. Rev. D 63 (6), 064029.
Greenspan, H. P., 1968. The Theory of Rotating Fluids. Cambridge University Press.
Hansen, C., Kawaler, S., 1994. Stellar interiors: Physical principles, structure and evolution. Springer.
Houdek, G., Rogl, J., Jun. 1996. On the accuracy of opacity interpolation schemes. Bulletin of the Astronomical Society of India 24, 317.
Hui-Bon-Hoa, A., Aug. 2008. The Toulouse Geneva Evolution Code (TGEC). Ast. Space Sc. 316, 55–60.
Jackson, S., MacGregor, K. B., Skumanich, A., May 2004. Models for the Rapidly Rotating Be Star Achernar. ApJ 606, 1196–1199.
Jackson, S., MacGregor, K. B., Skumanich, A., Feb. 2005. On the Use of the Self-consistent-Field Method in the Construction of Models for Rapidly Rotating Main-Sequence Stars. Astrophys. J. Supp. Ser. 156, 245–264.
James, R. A., Aug. 1964. The Structure and Stability of Rotating Gas Masses. ApJ 140, 552.
Kippenhahn, R., Weigert, A., 1990. Stellar structure and Evolution. Springer.
Kippenhahn, R., Weigert, A., Weiss, A., 2012. Stellar structure and Evolution. Springer.
Knoll, D. A., Keyes, D. E., Jan. 2004. Jacobian-free Newton-Krylov methods: a survey of approaches and applications. Journal of Computational Physics 193, 357–397.
Lemieux, J.-F., Price, S. F., Evans, K. J., Knoll, D., Salinger, A. G., Holland, D. M., Payne, A. J., Jul. 2011. Implementation of the Jacobian-free Newton-Krylov method for solving the first-order ice sheet momentum balance. Journal of Computational Physics 230, 6531–6545.
MacGregor, K. B., Jackson, S., Skumanich, A., Metcalfe, T. S., Jul. 2007. On the Structure and Properties of Differentially Rotating, Main-Sequence Stars in the 1-2 M_{solar} Range. ApJ 663, 560–572.
Maeder, A., 2009. Physics, Formation and Evolution of Rotating stars. Springer.
Monnier, J. D., Zhao, M., Pedretti, E., Thureau, N., Ireland, M., Muirhead, P., Berger, J.-P., Millan-Gabet, R., Van Belle, G., ten Brummelaar, T., McAlister, H., Ridgway, S., Turner, N., Sturmann, L., Sturmann, J., Berger, D., Jul. 2007. Imaging the Surface of Altair. Science 317, 342–.
Morel, P., 1997. CESAM: a code for stellar evolution calculations. A & A Suppl. Ser. 124, 597–614.
Morel, P., Lebreton, Y., Aug. 2008. CESAM: a free code for stellar evolution calculations. A & A Suppl. Ser. 316, 61–73.
Oliver, H. J., Reiman, A. H., Monticello, D. A., Jan. 2006. Solving the 3D MHD equilibrium equations in toroidal geometry by Newton's method. Journal of Computational Physics 211, 99–128.
Ostriker, J. P., Mark, J. W.-K., Mar. 1968. Rapidly rotating stars. I. The self-consistent-field method. ApJ 151, 1075–1088.
Paniconi, C., Putti, M., Dec. 1994. A comparison of Picard and Newton iteration in the numerical solution of multidimensional variably saturated flow problems. Water Resources Research 30, 3357–3374.
Paxton, B., Bildsten, L., Dotter, A., Herwig, F., Lesaffre, P., Timmes, F., Jan. 2011. Modules for Experiments in Stellar Astrophysics (MESA). Astrophys. J. Supp. Ser. 192, 3.
Rieutord, M., 2006a. The dynamics of the radiative envelope of rapidly rotating stars. i. a spherical boussinesq model. A&A 451, 1025–1036.
Rieutord, M., 2006b. Modeling rapidly rotating stars. In: Casoli, F., al. (Eds.), SF2A proceeding 2006. pp. astro–ph/0702384.
Rieutord, M., 2006c. On the dynamics of radiative zones in rotating star. In: Rieutord, M., Dubrulle, B. (Eds.), Stellar fluid dynamics and numerical simulations: From the sun to neutron stars. Vol. 21. EAS, pp. 275–295.
Rieutord, M., Espinosa Lara, F., 2009. On the dynamics of a radiative rapidly roating star. Comm. in Asteroseismology 158, 99–103.
Rieutord, M., Espinosa Lara, F., 2013. Ab Initio Modelling of Steady Rotating Stars. In: Goupil, M., Belkacem, K., Neiner, C., Lignières, F., Green, J. J. (Eds.), SeIsmology for studies of stellar Rotation and Convection. Vol. 865 of Lecture Notes in Physics, Berlin Springer Verlag. pp. 49–73, astro–ph/1208.4926.
Rogers, F. J., Swenson, F. J., Iglesias, C. A., Jan. 1996. OPAL Equation-of-State Tables for Astrophysical Applications. ApJ 456, 902.
Roxburgh, I. W., Dec. 2004. 2-dimensional models of rapidly rotating stars I. Uniformly rotating zero age main sequence stars. A&A 428, 171–179.
Roxburgh, I. W., Aug. 2006. 2-dimensional models of rapidly rotating stars. II. Hydrostatic and acoustic models with Ω=$\Omega(r,\theta)$. A&A 454, 883–888.
Sonneveld, P., 1989. CGS: A Fast Lanczos-Type Solver for Nonsymmetric Linear Systems. SIAM J. Sci. Statist. Comput. 10, 36–52.

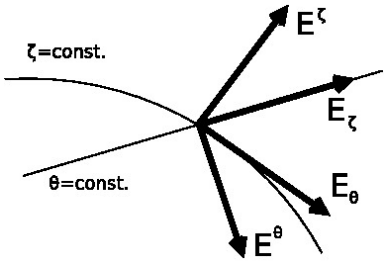

Figure A.12: Contravariant and covariant vectors of the meridional plane for the stellar models.

Xu, Y., Takahashi, K., Goriely, S., Arnould, M., Ohta, M., Utsunomiya, H., Nov. 2013. NACRE II: an update of the NACRE compilation of charged-particle-induced thermonuclear reaction rates for nuclei with mass number A<16. Nuclear Physics A 918, 61–169.

Appendix A. Some useful relations for the spheroidal geometry

Appendix A.1. Natural basis

We start by defining the natural basis for the spheroidal coordinates. We have two sets of basis vectors:

- Covariant basis vectors: $\mathbf{E}_i = \dfrac{\partial \mathbf{r}}{\partial x^i}$

$$\mathbf{E}_\zeta = r_\zeta \hat{\mathbf{r}}, \quad \mathbf{E}_\theta = r_\theta \hat{\mathbf{r}} + r\hat{\theta}, \quad \mathbf{E}_\varphi = r\sin\theta\hat{\varphi}, \tag{A.1}$$

- Contravariant basis vectors: $\mathbf{E}^i = \nabla x^i$

$$\mathbf{E}^\zeta = \frac{\hat{\mathbf{r}}}{r_\zeta} - \frac{r_\theta}{r r_\zeta}\hat{\theta}, \quad \mathbf{E}^\theta = \frac{\hat{\theta}}{r}, \quad \mathbf{E}^\varphi = \frac{\hat{\varphi}}{r\sin\theta}, \tag{A.2}$$

where $\hat{\mathbf{r}}, \hat{\theta}, \hat{\varphi}$ are the usual unit vectors in spherical coordinates, and

$$r_\zeta = \frac{\partial r}{\partial \zeta} \quad r_\theta = \frac{\partial r}{\partial \theta}$$

The vectors of the natural basis are not unit vectors. The covariant vector $\mathbf{E}_i$ is parallel to the line $x^j = \text{Cst}$, with $j \neq i$, while the contravariant vector $\mathbf{E}^i$ is perpendicular to the surface $x^i = \text{Cst}$. For orthogonal coordinates $\mathbf{E}_i$ and $\mathbf{E}^i$ are parallel, but this is not the case for non-orthogonal coordinates. In fig. A.12, we sketch out the $\mathbf{E}_i$ and $\mathbf{E}^i$ vectors in a meridional plane of the star.

The basis vectors satisfy

$$\mathbf{E}_i \cdot \mathbf{E}^j = \mathbf{E}^i \cdot \mathbf{E}_j = \delta_{ij} \tag{A.3}$$

where δ_{ij} is the Kronecker's delta.

Using the basis vectors, we can calculate the metric tensor

$$g_{ij} = \mathbf{E}_i \cdot \mathbf{E}_j = \begin{pmatrix} r_\zeta^2 & r_\zeta r_\theta & 0 \\ r_\zeta r_\theta & r^2 + r_\theta^2 & 0 \\ 0 & 0 & r^2 \sin^2\theta \end{pmatrix} \tag{A.4}$$

or, in contravariant form

$$g^{ij} = \mathbf{E}^i \cdot \mathbf{E}^j = \begin{pmatrix} \dfrac{r^2 + r_\theta^2}{r^2 r_\zeta^2} & \dfrac{-r_\theta}{r^2 r_\zeta} & 0 \\ \dfrac{-r_\theta}{r^2 r_\zeta} & \dfrac{1}{r^2} & 0 \\ 0 & 0 & \dfrac{1}{r^2 \sin^2\theta} \end{pmatrix} \tag{A.5}$$

Note that g^{ij} is the matrix inverse of g_{ij}, namely

$$g_{ij} g^{jk} = \delta_{ij}$$

where we have used the Einstein's summation convention, that implies summation over repeated indices.

Given two points x^i and $x^i + \mathrm{d}x^i$, the distance ($\mathrm{d}s$) between them is given by the metric tensor:

$$\mathrm{d}s^2 = g_{ij}\mathrm{d}x^i\mathrm{d}x^j = r_\zeta^2\mathrm{d}\zeta^2 + 2r_\zeta r_\theta \mathrm{d}\zeta\mathrm{d}\theta + (r^2 + r_\theta^2)\mathrm{d}\theta^2 + r^2\sin^2\theta\mathrm{d}\varphi^2 \tag{A.6}$$

The basis vectors verify

$$\mathbf{E}_i \cdot (\mathbf{E}_j \times \mathbf{E}_k) = \epsilon_{ijk} \tag{A.7}$$

and

$$\mathbf{E}^i \cdot (\mathbf{E}^j \times \mathbf{E}^k) = \epsilon^{ijk} \tag{A.8}$$

where ϵ^{ijk} is the Levi-Civita tensor

$$\epsilon_{ijk} = \sqrt{|g|}[i, j, k] \tag{A.9}$$

$$\epsilon^{ijk} = \frac{1}{\sqrt{|g|}}[i, j, k] \tag{A.10}$$

where $|g| = \det(g_{ij}) = r^4 r_\zeta^2 \sin^2\theta$ and

$$[i, j, k] = \begin{cases} 1 & \text{the arguments are an even permutation of } \zeta, \theta, \varphi \\ -1 & \text{the arguments are an odd permutation of } \zeta, \theta, \varphi \\ 0 & \text{two or more arguments are equal} \end{cases} \tag{A.11}$$

Appendix A.2. Representation of vectors

A vector $\mathbf{v}$ can be represented either in covariant or contravariant form:

- Covariant form: $\mathbf{v} = V_\zeta \mathbf{E}^\zeta + V_\theta \mathbf{E}^\theta + V_\varphi \mathbf{E}^\varphi$
- Contravariant form: $\mathbf{v} = V^\zeta \mathbf{E}_\zeta + V^\theta \mathbf{E}_\theta + V^\varphi \mathbf{E}_\varphi$

Here, V_i are the covariant components of the vector $\mathbf{v}$ and V^i the contravariant components. Note that

$$\mathbf{E}_i \cdot \mathbf{v} = V_i \qquad \text{and} \qquad \mathbf{E}^i \cdot \mathbf{v} = V^i$$

We can use the metric tensor to pass from one representation to the other, indeed

$$V_i = \mathbf{E}_i \cdot \mathbf{v} = \mathbf{E}_i \cdot (\mathbf{E}_j V^j) = g_{ij} V^j \tag{A.12}$$

and similarly

$$V^i = g^{ij} V_j \tag{A.13}$$

Let $(v_r, v_\theta, v_\varphi)$ be the spherical components of a vector $\mathbf{v}$ such that $\mathbf{v} = v_r \hat{\mathbf{r}} + v_\theta \hat{\theta} + v_\varphi \hat{\varphi}$. Its spheroidal components will be

$$V_\zeta = r_\zeta v_r, \quad V_\theta = r_\theta v_r + r v_\theta, \quad V_\varphi = r \sin\theta v_\varphi \tag{A.14}$$

and

$$V^\zeta = \frac{v_r}{r_\zeta} - \frac{r_\theta}{r r_\zeta} v_\theta, \quad V^\theta = \frac{v_\theta}{r}, \quad V^\varphi = \frac{v_\varphi}{r \sin\theta} \tag{A.15}$$

We can see from this expressions that V^θ an V^φ are in fact angular velocities.

Using the properties of the basis vectors it can be shown that the scalar product of two vectors is given by

$$\mathbf{a} \cdot \mathbf{b} = A_i B^i = A^i B_i \tag{A.16}$$

and the cross product is

$$\begin{aligned} (\mathbf{a} \times \mathbf{b})^i &= \epsilon^{ijk} A_j B_k \\ (\mathbf{a} \times \mathbf{b})_i &= \epsilon_{ijk} A^j B^k \end{aligned} \tag{A.17}$$

After the presentation of the basics of the representation of vectors in spheroidal coordinates, let's see now a little example. Consider a surface $\mathcal{S}$ defined by $\zeta = \text{Cst}$ as for example the surface of a star or the frontier between two subdomains. We want to calculate the normal and tangential projections of a vector $\mathbf{v}$ with respect to $\mathcal{S}$. First, we define a unit vector $\hat{\mathbf{n}}$, perpendicular to $\mathcal{S}$. For that, we just recall that $\mathbf{E}^\zeta$ is perpendicular to the surfaces $\zeta = \text{Cst}$, but it is not a unit vector, so

$$\hat{\mathbf{n}} = \frac{\mathbf{E}^\zeta}{|\mathbf{E}^\zeta|} = \frac{\mathbf{E}^\zeta}{\sqrt{\mathbf{E}^\zeta \cdot \mathbf{E}^\zeta}} = \frac{\mathbf{E}^\zeta}{\sqrt{g^{\zeta\zeta}}} \tag{A.18}$$

then, the normal projection is

$$\hat{\mathbf{n}} \cdot \mathbf{v} = \frac{V^\zeta}{\sqrt{g^{\zeta\zeta}}} = \frac{r_\zeta V^\zeta}{\sqrt{1 + \frac{r_\theta^2}{r^2}}} \tag{A.19}$$

For the parallel projection we have two vectors, the first one, in the direction of φ is just the spherical unit vector $\hat{\varphi}$, in the latitudinal direction, however, it will be

$$\hat{\mathbf{t}} = \frac{\mathbf{E}_\theta}{|\mathbf{E}_\theta|} = \frac{\mathbf{E}_\theta}{\sqrt{\mathbf{E}_\theta \cdot \mathbf{E}_\theta}} = \frac{\mathbf{E}_\theta}{\sqrt{g_{\theta\theta}}} \tag{A.20}$$

so, the parallel projections over $\mathcal{S}$ are

$$\hat{\mathbf{t}} \cdot \mathbf{v} = \frac{V_\theta}{\sqrt{g_{\theta\theta}}} = \frac{1}{\sqrt{1 + \frac{r_\theta^2}{r^2}}} \frac{V_\theta}{r} \tag{A.21}$$

and

$$\hat{\varphi} \cdot \mathbf{v} = \frac{V_\varphi}{r \sin\theta} \tag{A.22}$$

Appendix A.3. Tensors

A second order tensor $\mathcal{T}$ is represented using 2 indices

$$\mathcal{T} = T^{ij}\mathbf{E}_i\mathbf{E}_j = T_{ij}\mathbf{E}^i\mathbf{E}^j = T^i{}_j\mathbf{E}_i\mathbf{E}^j = T_i{}^j\mathbf{E}^i\mathbf{E}_j \tag{A.23}$$

Again, we can use the metric tensor to lower and raise indices

$$\begin{aligned} T^{ij} &= g^{ik}T_k{}^j = g^{jl}T^i{}_l = g^{ik}g^{jl}T_{kl} \\ T_{ij} &= g_{ik}T^k{}_j = g_{jl}T_i{}^l = g_{ik}g_{jl}T^{kl} \end{aligned} \tag{A.24}$$

The tensor product of 2 vectors is a tensor

$$(\mathbf{a}\ \mathbf{b})^{ij} = a^i b^j \tag{A.25}$$

The dot product between a tensor and a vector is

$$(\mathcal{T} \cdot \mathbf{v})^i = T^{ij}V_j \tag{A.26}$$

and between a vector and a tensor

$$(\mathbf{v} \cdot \mathcal{T})^j = T^{ij}V_i \tag{A.27}$$

Finally, the double dot product is a scalar

$$\mathcal{T} : \mathcal{T} = T^{ij}T_{ij} \tag{A.28}$$

All of this can be generalized to higher order tensors.

Appendix A.4. Differential operators

Our goal is to be able to write differential equations using spheroidal coordinates. For that, we start finding the relation between the partial derivatives with respect to the spherical coordinates and those calculated with respect to the spheroidal coordinates. To clarify the notation, we add a prime ($'$) to the spheroidal θ' and φ' coordinates. Thus, the derivative with respect to a spheroidal coordinate is done holding the other spheroidal coordinates constant. Following the chain rule

$$\frac{\partial}{\partial r} = \frac{\partial\zeta}{\partial r}\frac{\partial}{\partial\zeta} + \frac{\partial\theta'}{\partial r}\frac{\partial}{\partial\theta'} + \frac{\partial\varphi'}{\partial r}\frac{\partial}{\partial\varphi'} \tag{A.29}$$

Obviously, $\dfrac{\partial\theta'}{\partial r} = \dfrac{\partial\varphi'}{\partial r} = 0$, and

$$\mathrm{d}r = r_\zeta \mathrm{d}\zeta + r_\theta \mathrm{d}\theta, \qquad \mathrm{d}\zeta = \frac{1}{r_\zeta}\mathrm{d}r - \frac{r_\theta}{r_\zeta}\mathrm{d}\theta$$

where we see that $\dfrac{\partial \zeta}{\partial r} = \dfrac{1}{r_\zeta}$ and $\dfrac{\partial \zeta}{\partial \theta} = -\dfrac{r_\theta}{r_\zeta}$. Then

$$\frac{\partial}{\partial r} = \frac{1}{r_\zeta}\frac{\partial}{\partial \zeta} \tag{A.30}$$

The other partial derivatives are calculated in the same way

$$\frac{\partial}{\partial \theta} = \frac{\partial}{\partial \theta'} - \frac{r_\theta}{r_\zeta}\frac{\partial}{\partial \zeta} \qquad \text{and} \qquad \frac{\partial}{\partial \varphi} = \frac{\partial}{\partial \varphi'} \tag{A.31}$$

Of course, we could substitute these expressions into the expressions of the differential operators written with the spherical coordinates, but there is a much more efficient way to do it.

First, let's define the general form of the gradient of a scalar quantity. The gradient is a vector, whose covariant components are

$$(\nabla \phi)_i = \frac{\partial \phi}{\partial x^i} = \phi_{,i} \tag{A.32}$$

where we have introduced the comma notation for the partial derivative. The contravariant components of the gradient will be

$$(\nabla \phi)^i = g^{ij}\phi_{,j} \tag{A.33}$$

We can also derive a component of a vector V^i in the same way. However, this derivative

$$\frac{\partial V^i}{\partial x^j} = V^i{}_{,j} \tag{A.34}$$

is not a tensor, as it does not transform as a tensor under a change of coordinates. That's why one introduces the covariant derivative

$$\nabla_j V^i = V^i{}_{;j} = V^i{}_{,j} + \Gamma^i{}_{kj} V^k \tag{A.35}$$

where $\Gamma^i{}_{kj} = \mathbf{E}^i \cdot \dfrac{\partial \mathbf{E}_k}{\partial x^j}$ is a Christoffel symbol of the second kind. The covariant derivative of a vector $V^i{}_{;j}$ is a tensor that represents the gradient of the vector.

$$(\nabla \mathbf{v})^{ij} = g^{jk}(\nabla \mathbf{v})^i{}_k = g^{jk} V^i{}_{;k} \tag{A.36}$$

We can also calculate the covariant derivative using the covariant components of the vector

$$\nabla_j V_i = V_{i;j} = V_{i,j} - \Gamma^k{}_{ij} V_k \tag{A.37}$$

The Christoffel symbols can be calculated using the following relation

$$\Gamma^i_{jk} = \frac{1}{2} g^{il}(g_{lj,k} + g_{lk,j} - g_{jk,l}) \tag{A.38}$$

where we see that they are symmetric with respect to the second and third indices $\Gamma^i_{jk} = \Gamma^i_{kj}$. They also verify

$$\Gamma^i_{ji} = \frac{\partial \ln \sqrt{|g|}}{\partial x^j} \tag{A.39}$$

The covariant derivative of second order tensors is obtained in a similar way

$$\nabla_k T^{ij} = T^{ij}{}_{;k} = T^{ij}{}_{,k} + \Gamma^i{}_{lk} T^{lj} + \Gamma^j{}_{lk} T^{il} \tag{A.40}$$

If one of the indices is covariant, then we have

$$\nabla_k T^i{}_j = T^i{}_{j;k} = T^i{}_{j,k} + \Gamma^i{}_{lk} T^l{}_j - \Gamma^l{}_{jk} T^i{}_l \tag{A.41}$$

where we can see the general rule valid also for higher order tensors, the covariant derivative is equal to the regular derivative plus:

- for each contravariant index, $+\Gamma^i{}_{lk} T^{\dots l \dots}$
- for each covariant index, $-\Gamma^l{}_{ik} T_{\dots l \dots}$

Using the covariant derivative, we can calculate all the differential operators in spheroidal coordinates. Hence, the divergence of a vector is

$$\nabla \cdot \mathbf{v} = \nabla_i V^i = V^i{}_{;i} \tag{A.42}$$

and of a tensor

$$(\nabla \cdot \mathcal{T})^i = \nabla_j T^{ij} = T^{ij}{}_{;j} \tag{A.43}$$

Note that some authors prefer the definition $(\nabla \cdot \mathcal{T})^j = \nabla_i T^{ij} = T^{ij}{}_{;i}$, which is summed over the first index. Using the expression for the cross product, we can calculate the curl of a vector

$$(\nabla \times \mathbf{v})^i = \epsilon^{ijk} \nabla_j V_k = \epsilon^{ijk} V_{k;j} \tag{A.44}$$

The Laplacian of a scalar field is

$$\nabla^2 \phi = \nabla \cdot (\nabla \phi) = \nabla_i (g^{ij} \nabla_j \phi) = (g^{ij} \phi_{,j})_{;i} \tag{A.45}$$

and for a vector field

$$(\nabla^2 \mathbf{v})^i = \nabla_j (g^{jk} \nabla_k V^i) = (g^{jk} V^i{}_{;k})_{;j} \tag{A.46}$$

The material derivative is

$$[(\mathbf{v} \cdot \nabla)\mathbf{v}]^i = V^j \nabla_j V^i = V^j V^i{}_{;j} \tag{A.47}$$

Appendix A.5. Other relations

- Line, area and volume elements
  - Line element

$$\mathrm{d}s^2 = g_{ij} \mathrm{d}x^i \mathrm{d}x^j = r_\zeta^2 \mathrm{d}\zeta^2 + 2 r_\zeta r_\theta \mathrm{d}\zeta \mathrm{d}\theta + (r^2 + r_\theta^2) \mathrm{d}\theta^2 + r^2 \sin^2\theta \mathrm{d}\varphi^2 \tag{A.48}$$

$$\mathrm{d}\mathbf{r} = \mathbf{E}_i \mathrm{d}x^j = \mathbf{E}_\zeta \mathrm{d}\zeta + \mathbf{E}_\theta \mathrm{d}\theta + \mathbf{E}_\varphi \mathrm{d}\varphi \tag{A.49}$$

  - Area element in a surface ζ =const.

$$\mathrm{d}\mathbf{S} = (\mathbf{E}_\theta \times \mathbf{E}_\varphi) \mathrm{d}\theta \mathrm{d}\varphi = r^2 r_\zeta \sin\theta \mathbf{E}^\zeta \mathrm{d}\theta \mathrm{d}\varphi \tag{A.50}$$

$$\mathrm{d}S = |\mathrm{d}\mathbf{S}| = \sqrt{g^{\zeta\zeta}} r^2 r_\zeta \sin\theta \mathrm{d}\theta \mathrm{d}\varphi = r^2 \sqrt{1 + \frac{r_\theta^2}{r^2}} \sin\theta \mathrm{d}\theta \mathrm{d}\varphi \tag{A.51}$$

– Area element in a surface of constant $p = p(\zeta, \theta)$.

$$\mathrm{d}\mathbf{S} = r^2 r_\zeta \sin\theta \left(\mathbf{E}^\zeta + \frac{p_{,\theta}}{p_{,\zeta}} \mathbf{E}^\theta \right) \mathrm{d}\theta \mathrm{d}\varphi \tag{A.52}$$

$$\mathrm{d}S = |\mathrm{d}\mathbf{S}| = r^2 r_\zeta \sin\theta \sqrt{g^{\zeta\zeta} + 2\frac{p_{,\theta}}{p_{,\zeta}} g^{\zeta\theta} + \left(\frac{p_{,\theta}}{p_{,\zeta}} \right)^2 g^{\theta\theta}} \mathrm{d}\theta \mathrm{d}\varphi \tag{A.53}$$

– Volume element

$$\mathrm{d}V = \mathbf{E}_\zeta \cdot (\mathbf{E}_\theta \times \mathbf{E}_\varphi) \mathrm{d}\zeta \mathrm{d}\theta \mathrm{d}\varphi = r^2 r_\zeta \sin\theta \mathrm{d}\zeta \mathrm{d}\theta \mathrm{d}\varphi \tag{A.54}$$

- Differential operators

– Gradient

$$\nabla\phi = \phi_{,i} \mathbf{E}^i = \frac{\partial\phi}{\partial\zeta} \mathbf{E}^\zeta + \frac{\partial\phi}{\partial\theta} \mathbf{E}^\theta + \frac{\partial\phi}{\partial\varphi} \mathbf{E}^\varphi \tag{A.55}$$

– Divergence

$$\begin{aligned} \nabla \cdot \mathbf{v} &= V^i{}_{;i} = \frac{\partial V^i}{\partial x^i} + \frac{\partial \ln\sqrt{|g|}}{\partial x^k} V^k = \\ &= \frac{\partial V^\zeta}{\partial\zeta} + \left(\frac{2r_\zeta}{r} + \frac{r_{\zeta\zeta}}{r_\zeta} \right) V^\zeta + \frac{\partial V^\theta}{\partial\theta} + \left(\frac{2r_\theta}{r} + \frac{\cos\theta}{\sin\theta} + \frac{r_{\zeta\theta}}{r_\zeta} \right) V^\theta + \frac{\partial V^\varphi}{\partial\varphi} \end{aligned} \tag{A.56}$$

– Laplacian

$$\begin{aligned} \nabla^2\phi &= \mathrm{Div}(\nabla\phi) = (g^{ij}\phi_{,j})_{;i} = \frac{1}{\sqrt{|g|}} \frac{\partial}{\partial x^i} \left(\sqrt{|g|} g^{ij} \frac{\partial\phi}{\partial x^j} \right) = \\ &= g^{\zeta\zeta} \frac{\partial^2\phi}{\partial\zeta^2} + 2g^{\zeta\theta} \frac{\partial^2\phi}{\partial\zeta\partial\theta} + \frac{1}{r^2} \frac{\partial^2\phi}{\partial\theta^2} + \frac{1}{r^2 \sin^2\theta} \frac{\partial^2\phi}{\partial\varphi^2} + \\ &\quad + \left[\frac{2}{r r_\zeta} - \frac{r_{\theta\theta}}{r^2 r_\zeta} - g^{\zeta\zeta} \frac{r_{\zeta\zeta}}{r_\zeta} - g^{\zeta\theta} \left(\frac{2r_{\zeta\theta}}{r_\zeta} - \frac{\cos\theta}{\sin\theta} \right) \right] \frac{\partial\phi}{\partial\zeta} + \frac{\cos\theta}{r^2 \sin\theta} \frac{\partial\phi}{\partial\theta} \end{aligned} \tag{A.57}$$

– Curl

$$\begin{aligned} \nabla \times \mathbf{v} &= \epsilon^{ijk} V_{k;j} \mathbf{E}_i = \\ &= \frac{1}{r^2 r_\zeta \sin\theta} \left[\left(\frac{\partial V_\varphi}{\partial\theta} - \frac{\partial V_\theta}{\partial\varphi} \right) \mathbf{E}_\zeta + \left(\frac{\partial V_\zeta}{\partial\varphi} - \frac{\partial V_\varphi}{\partial\zeta} \right) \mathbf{E}_\theta + \left(\frac{\partial V_\theta}{\partial\zeta} - \frac{\partial V_\zeta}{\partial\theta} \right) \mathbf{E}_\varphi \right] \end{aligned} \tag{A.58}$$

– Material derivative

$$
\begin{aligned}
&(\mathbf{a}\cdot\nabla)\mathbf{b} = A^j B^i{}_{;j}\mathbf{E}_i = \\
&= \left[A^\zeta\frac{\partial B^\zeta}{\partial\zeta} + A^\theta\frac{\partial B^\zeta}{\partial\theta} + A^\varphi\frac{\partial B^\zeta}{\partial\varphi} + \frac{r_{\zeta\zeta}}{r_\zeta}A^\zeta B^\zeta + \left(\frac{r_{\zeta\theta}}{r_\zeta} - \frac{r_\theta}{r}\right)\left(A^\zeta B^\theta + A^\theta B^\zeta\right) + \right. \\
&\left. + \frac{1}{r_\zeta}\left(r_{\theta\theta} - \frac{2r_\theta^2}{r} - r\right)A^\theta B^\theta + \frac{\sin\theta}{r_\zeta}\left(r_\theta\cos\theta - r\sin\theta\right)A^\varphi B^\varphi\right]\mathbf{E}_\zeta + \\
&+ \left[A^\zeta\frac{\partial B^\theta}{\partial\zeta} + A^\theta\frac{\partial B^\theta}{\partial\theta} + A^\varphi\frac{\partial B^\theta}{\partial\varphi} + \frac{r_\zeta}{r}\left(A^\zeta B^\theta + A^\theta B^\zeta\right) + \frac{2r_\theta}{r}A^\theta B^\theta - \sin\theta\cos\theta A^\varphi B^\varphi\right]\mathbf{E}_\theta + \\
&+ \left[A^\zeta\frac{\partial B^\varphi}{\partial\zeta} + A^\theta\frac{\partial B^\varphi}{\partial\theta} + A^\varphi\frac{\partial B^\varphi}{\partial\varphi} + \frac{r_\zeta}{r}\left(A^\zeta B^\varphi + A^\varphi B^\zeta\right) + \left(\frac{r_\theta}{r} + \frac{\cos\theta}{\sin\theta}\right)\left(A^\theta B^\varphi + A^\varphi B^\theta\right)\right]\mathbf{E}_\varphi
\end{aligned}
\tag{A.59}
$$

- Christoffel symbols (different from 0)

$$
\begin{array}{lll}
\Gamma^\zeta_{\zeta\zeta} = \dfrac{r_{\zeta\zeta}}{r_\zeta} & \Gamma^\zeta_{\zeta\theta} = \dfrac{r_{\zeta\theta}}{r_\zeta} - \dfrac{r_\theta}{r} & \Gamma^\zeta_{\theta\theta} = \dfrac{1}{r_\zeta}\left(r_{\theta\theta} - \dfrac{2r_\theta^2}{r} - r\right) \\
\Gamma^\zeta_{\varphi\varphi} = \dfrac{\sin\theta}{r_\zeta}(r_\theta\cos\theta - r\sin\theta) & \Gamma^\theta_{\zeta\theta} = \dfrac{r_\zeta}{r} & \Gamma^\theta_{\theta\theta} = \dfrac{2r_\theta}{r} \\
\Gamma^\theta_{\varphi\varphi} = -\sin\theta\cos\theta & \Gamma^\varphi_{\zeta\varphi} = \dfrac{r_\zeta}{r} & \Gamma^\varphi_{\theta\varphi} = \dfrac{r_\theta}{r} + \dfrac{\cos\theta}{\sin\theta}
\end{array}
\tag{A.60}
$$

where $\Gamma^i_{jk} = \Gamma^i_{kj}$ should be used for the remaining ones.